August 26, 2019

VIV of flexible structures in 2D uniform flow

Abstract

The paper investigates Vortex-Induced Vibration (VIV) of a horizontal flexible structure with pinned-pinned ends in uniform flow. The fluid - structure interaction is modelled using the wake oscillator approach to describe fluctuations of the fluid forces based on the results, previously reported by (Pavlovskaia *et al.*, 2016), (Postnikov *et al.*, 2016), (Kurushina *et al.*, 2018). New two-dimensional wake oscillator models are developed in this study employing a number of alternative damping types in the fluid equation. The proposed models are calibrated with the published experimental data by (Sanaati and Kato, 2012), for VIV of a horizontal flexible structure for the middle cross-section. The calibration is performed with the focus on the maximum of the observed displacement amplitude in the cross-flow direction. One of the models having the Van der Pol - Krenk-Nielsen damping allowed achieving the lowest objective function during the calibration and, hence, was selected for the detailed analysis in 3 and 5 mode approximations. The dynamics of this model is considered in terms of the time histories, changes in the standard deviations of the modal coefficients along the reduced velocity range and frequency response. Also, a comparison with the alternative model versions in terms of the displacements generated at different locations is provided.

In contrast to the previous findings by (Kurushina *et al.*, 2018) for VIV of rigid structures, for the flexible structures it was found in this study that both Van der Pol and Rayleigh damping types appear to be applicable for the VIVs prediction. A detailed consideration of the 3 mode approximation of the Krenk-Nielsen - Van der Pol model reveals a presence of co-existing solutions in a number of regions of the reduced velocity. They are present in short ranges of reduced velocity in between the lock-in peaks of the in-line displacement coefficient of the first mode. Modulations and co-existing solutions in the in-line modal coefficients make the in-line displacement prediction challenging while the cross-flow displacement amplitudes are described reasonably well by the proposed models.

Keywords: Vortex-Induced Vibrations, wake oscillator model, flexible structure, uniform flow, model calibration, co-existing solutions

1 Introduction

Application of flexible structures is related to the progress of subsea production industry which is focused on extraction of oil and gas resources from greater ocean depths. The offshore production systems currently can operate in depth over 2000 m by using systems of flexible risers, flowlines and umbilicals. As any other slender body, flexible offshore structures experience interactions with the flow caused by waves at the proximity of the free water surface and deep water currents. For a structure, an increase of the vibration amplitude, when the vortex shedding frequency is near one of the natural frequencies of the structure, is defined as a "resonance", where the fluid motion represents the source of external excitation.

The vortex shedding frequency of a fixed structure is dependent on the flow velocity and the Strouhal number, which is approximately constant for a wide range of Reynolds numbers [1]. When the vortex shedding frequency approaches the natural frequency of a structure which is considered as a cylinder, it becomes "locked-in", which means it keeps constant the vibration frequency and does not follow the Strouhal relationship for a

range of the flow velocity [2]. This state is referred in the literature as "lock-in" or "synchronisation" between the vortex shedding process and the structural motion, where large displacement amplitudes ("near-resonance vibration") are often observed within the lock-in regime [2].

Ability to learn from the experimental data is critical for improving the fundamental understanding of vortex-induced vibrations. The difference between low and high mass ratio structures originates from experiments and is widely discussed (see, for example, [3, 4]), allowed to calibrate semi-empirical models using the mass ratio as important parameter [5, 6]. In our view, an enhancement to the prediction accuracy of VIV for flexible structures, should be based on the qualitative patterns identified by analysing experimental data as, for example, discussed in [7] or in [8]. Two types of structural response during VIVs have been revealed in [8] by scrutinizing the recorded signals, where one shows periodic or quasi-periodic responses, and another indicates chaotic vibrations. These response types have been defined in [8] as a mixture of the excited mode shapes with static nodal points and the mode shapes with nodal points propagating along the structure. A different proportion of these two types of modes, according to [8], defines whether the resulting structural motion is more periodic (if the first type dominates) or chaotic (if the second type prevails).

Structures are considered rigid in VIV studies, if only one mode can be excited, and as flexible, if two or more harmonics can potentially come into the synchronization (lock-in) with drag and lift forces of external fluid. Experimental studies of vortex-induced vibrations in flexible structures have been attracting attention of the research community over the last three decades. The work by Alexander [9] was one of the first with the long wire (a flexible structure), which was investigated both in the laboratory and in the field conditions. The study reported overall lower cross-flow displacement amplitudes than for low aspect ratio structures based on the data available at that time.

The author of [7] investigated a horizontal flexible structure in sheared flow and discussed the conditions when a single-mode lock-in, a multi-mode lock-in or non-lock-in state can be observed. It was highlighted that a multi-mode response with the static nodal and antinodal points is likely to occur on the low aspect ratio structures. The study showed that the propagation of the nodal and antinodal points along the structure increases with the increase of the aspect ratio. A multi-mode lock-in can be characterised with lower displacement amplitudes than a single-mode lock-in, and the number of the potentially excited modes depends on how many natural frequencies of multiple modes fall into the interval of the vortex shedding frequency. Infinitely long structures with multi-mode lock-in were considered in the study [10] and modelled using the structural, hydrodynamic and wave radiation dampings, varied spatially along their lengths.

A comparison of the observed lock-in behaviour of a flexible structure and a 1DOF rigid structure is presented in [11]. These results are similar to the previously reported in [7, 9], although, the flexible structure demonstrated higher displacement amplitudes than the 1DOF rigid structures. The increase in the displacement amplitude for the reduced velocity exceeding 12.0 was observed in [11] and was named the "high-speed mode", as this mode was present only for the increasing flow velocity. Studies on flexible and rigid structures has also been extended to VIV mitigation. For example, investigation in [12] was focused on a horizontal flexible structure VIV with and without helical strakes, and it was shown that the suppression is less effective for a flexible structure than it is for a rigid structure.

Responses of flexible structures appear more complex than for rigid structures, that manifests also in the relationship of in-line and cross-flow displacement amplitudes. The vibrations of a long flexible horizontal structure in uniform flow were investigated in [13], where up to 6 and 12 modes for the cross-flow and in-line directions, respectively, were observed. The in-line and cross-flow displacement amplitudes were obtained to be of the same order, that is clearly different from the relationships typical for rigid structures, where in-line

displacement amplitudes can be 10 times lower than cross-flow amplitudes (see, for example, [14]). Also, the responses recorded in [13] were asymmetrical relatively the pipe length, and the authors considered them as a product of different modal amplitudes, modal frequencies and phase differences between modes.

Vertical structures experiencing VIV were considered in [15, 16] for the stepped and in [17–19] for the uniform flows. The authors of [16] found the amplitudes of the in-line oscillations to be of the same order as the cross-flow oscillations. The work reported in [17] considered low mode numbers and the hysteresis effect in terms of each mode, and the even modes were not observed in the in-line direction, under the symmetric loading. Horizontal structure in oscillatory flow was considered in [20].

Although a significant amount of experimental data is available, there are no robust theoretical models of vortex-induced vibrations, which would allow accurate predictions for all the known cases. Time-consuming computational fluid dynamics (CFD) is currently one of the ways to determine accurately the values of fluctuating fluid forces and resulting motion of the considered structures. By solving the Navier-Stokes equations, CFD codes calculate the variables of the boundary layer of the fluid around structure simulating the process of vortex formation and tracking changes in the pressure, velocity, vorticity fields which affect the lift and drag forces acting on slender structures. For example, one of the recent works in this area, [21], considered a flexible three-dimensional riser using ANSYS software and achieved agreement for four velocity profiles (two uniform, two sheared) with the data [22]. A couple of other works, [23, 24], applied different CFD codes for the cases of zero damping elastically-supported rigid structures at low Reynolds number. The definite advantage of CFD is the capability to consider various structural geometry, flows of different angles relatively the structures, time-dependent flows, different boundary conditions and to vary a number of structures. The difficulty here is that increasing the complexity of the case, presenting the structure(s) and flow(s) in more details requires more cells in the mesh as discretisation of the considered space and more time steps or iterations at the solution stage, especially, for turbulent or sheared flow. Thus, CFD often arrives to solving hundreds of thousands equations simultaneously, which can be sometimes reduced by adaptive meshing based on the results of the previous step. Despite of the accuracy advantages and adaptability of CFD for various cases, the complexity of this method makes the strong argument to develop phenomenological (semi-empirical) models.

In our view, the main reason why the semi-empirical VIV models are not robust enough is a lack of effort for calibration of the existing models and developing new ones. Calibration can be designed using the expensive experimental data or the CFD-generated data for a number of cases (see, for example, [25]). Calibrated phenomenological models can be implemented in the software, as for example, they are in Orcaflex [26], where a few alternative methods (wake oscillator, vortex tracking, framework for Shear7 [27]) are suggested to the user for VIV prediction.

One of the phenomenological approaches to model VIV problems utilises nonlinear oscillators with a self-excited and self-limited cycle as a mean to imitate fluctuations of the lift and drag forces acting on the structure. From this perspective, observed patterns of vortex formation and changes in the boundary layer do not play a role in the final predictions of displacements and forces. The ideas of this approach have been conceived around fifty years ago, and the notable publications include [28, 29]. The strength of wake oscillators is their simplicity, which is a weakness at the same time: the link to reality has to be constructed carefully through the set of empirical coefficients.

The mathematical apparatus of wake oscillator methods has evolved during the past 20 years, and at the present time, it includes number of fluid equations [30]; coupling terms between the structural and the fluid equation [31] and between two fluid equations [32]; frequency-dependent coefficients [33]; nonlinear terms in structural equation [34]; various nonlinear damping terms in the fluid equation as proposed and explored in

[6, 35–39]. Tuning the empirical coefficients was discussed in [5, 34, 39–42]. Majority of these tools have been applied to model the rigid structures with one or two degrees-of-freedom in uniform flows. The recent wake oscillator models of flexible structures were suggested in [43, 44]. Viable semi-empirical method, as an alternative to wake oscillator in the future, is application of neural networks for VIV problem, suggested in [45] for top-tensioned risers.

The work presented in this paper aims to develop a wake oscillator based model to describe VIVs of a flexible structure in two dimensions and for different cross-sections. Here, the various nonlinear damping types will be compared, and the developed suite of mathematical models will be calibrated with the published experimental data. The case of the uniform flow and the relatively short structures is the focus of this investigation. Mathematical formulation is based on the previously proposed models for one-dimensional flexible structure VIV in [46, 47], and experimental data employed for the model calibration have been obtained by Sanaati and Kato [48] for the horizontally positioned flexible structure.

The rest of the paper is organised as follows. Section 2 provides details of the new two-dimensional model of a flexible structure, capable of oscillating in both in-line and cross-flow directions. Section 3 describes the model calibration procedure and the results for 28 versions of the proposed model. The properties of a selected models based on Krenk-Nielsen and Van der Pol equations are considered in Section 4. A further comparison of the calibrated model versions is given in Section 5. Section 6 discusses the results of the conducted research and opportunities to improve the prediction of vortex-induced vibrations of flexible structures.

2 Mathematical modelling and fluid nonlinearities

Cross-flow and in-line vibrations of flexible structure subjected to the uniform flow are considered in this study. The structure is positioned in vertical or horizontal configuration as shown in Fig. 1, and the two displacements x and y (in-line and cross-flow) are calculated whereas axial motion in $\bar{Z}$ direction is not considered. The approach employed in [46] for structures moving in cross-flow direction only is developed here for the case of both in-line and cross-flow vibrations.

To be able to describe a real submerged slender structure in the vertical or near vertical position and compare with the field measurements, it is essential to work in the effective tension - apparent weight space [49]. This space accounts for the pressure of the internal and the displaced external fluid and its variation along the significant structural length. The focus of the current work is on the occurrence and development of the lock-in state for structures in the air using the structural equation as appears in [46] and the fluid equation with the calibrated empirical constants. This approach appears to be sufficiently accurate to simulate VIVs as they develop in the laboratory conditions as in [48]. However, for the future analysis of the real systems the apparent weight and effective tension will be required to be taken into account.

Euler-Bernoulli beam equation is used to describe the vibration of a flexible structure positioned vertically:

$$m_* \frac{\partial^2 \vec{r}(\bar{Z},t)}{\partial t^2} + EI \frac{\partial^4 \vec{r}(\bar{Z},t)}{\partial \bar{Z}^4} - \frac{\partial}{\partial \bar{Z}}\left(T \frac{\partial \vec{r}(\bar{Z},t)}{\partial \bar{Z}}\right) = \vec{F}_F(\bar{Z},t). \tag{1}$$

Here, m_* is mass per unit length including structural mass (and mass of internal fluid if applicable) and fluid added mass, EI is bending stiffness, T is the tension at the cross-section, $\vec{r}$ is the vector of displacement of the structure, and $\vec{F}_F$ is the vector of fluid forces acting on the structure. The displacement vector and forcing vector depend on time t and location on the beam $\bar{Z}$, which constitutes the distance from the bottom end of the beam up to the considered cross-section. The tension T at the location $\bar{Z}$ along the beam is defined as $T = T_b + W_w \bar{Z}$, where T_b is tension at the bottom of the vertical structure or $T_b = T_0 - W_w L$ with T_0 being the pretension applied to the top end as shown in Fig. 1b, and W_w is the structural weight per unit length. For

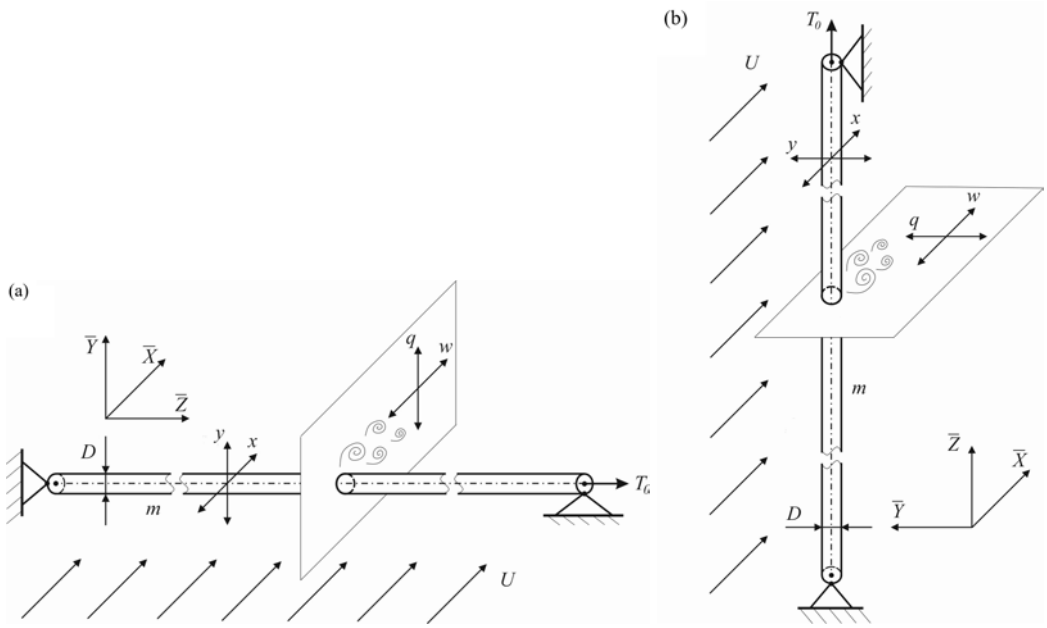

Figure 1: Two-dimensional flexible structure interacting with the uniform flow of velocity U: (a) in horizontal arrangement; (b) in vertical arrangement. Here, D is structural diameter, m is structural mass per unit length, q and w are wake coefficients, x and y are displacements of the structure, and T_0 is tension applied at the top of vertical structure or at the one side of the horizontal structure.

the horizontal structure (as shown in Fig. 1a), the influence of the structural weight per unit length is being neglected, because the weight and the pretension T_0 are perpendicular to each other in this case, and therefore, the total tension is $T = T_b = T_0$.

Displacement vector is defined as $\vec{r} = x\vec{i} + y\vec{j}$, where $\vec{i}$ and $\vec{j}$ are unit vectors along the in-line axis $\overline{X}$ and cross-flow axis $\overline{Y}$, respectively. Therefore Eq.(1) can be re-written as:

$$m_*\ddot{x} + EIx'''' - (T_b + W_w\bar{Z})x'' - (W_w)x' = (\vec{F}_F)_X, \tag{2}$$

$$m_*\ddot{y} + EIy'''' - (T_b + W_w\bar{Z})y'' - (W_w)y' = (\vec{F}_F)_Y, \tag{3}$$

where dot denotes differentiation with respect to time, and prime represents differentiation with respect to coordinate $\overline{Z}$. $(\vec{F}_F)_X$ and $(\vec{F}_F)_Y$ are projections of the total fluid force on the axes $\overline{X}$ and $\overline{Y}$.

The total fluid force can be represented as a sum of the lift and drag forces $\vec{F}_L$ and $\vec{F}_D$:

$$\vec{F}_F(\bar{Z}, t) = \vec{F}_L + \vec{F}_D. \tag{4}$$

The drag force is defined as:

$$\vec{F}_D = \frac{\rho_F C_D D}{2}|\vec{U}_{rel}|\vec{U}_{rel}, \tag{5}$$

where C_D is a drag coefficient, ρ_F is fluid density, D is cylinder diameter, and $\vec{U}_{rel}$ is relative velocity of the flow around cylinder:

$$\vec{U}_{rel} = \Big(U - \frac{\partial x(\bar{Z}, t)}{\partial t}\Big)\vec{\imath} - \frac{\partial y(\bar{Z}, t)}{\partial t}\vec{j}, \tag{6}$$

where U is velocity of the flow in direction $\overline{X}$. In this case, the relative velocity of the flow $\vec{U}_{rel}$ determines the direction of the drag force, which is always opposite the cylinder motion.

The drag coefficient is assumed to be a sum of the initial mean drag coefficient, C_{D0} and fluctuating drag coefficient, C_D^{fl}:

$$C_D = C_{D0} + C_D^{fl}. \tag{7}$$

The lift force is calculated as proposed in [25, 46]:

$$\vec{F}_L = \frac{\rho_F D}{2} C_L |\vec{U}_{rel}|^2 \mathbf{R}\left(\frac{\pi}{2}, \vec{k}\right) \cdot \frac{\vec{U}_{rel}}{|\vec{U}_{rel}|}; \tag{8}$$

where C_L is the lift coefficient and $\mathbf{R}(\frac{\pi}{2}, \vec{k})$ is the tensor of rotation which turns the relative velocity vector $\vec{U}_{rel}$ in a counterclockwise direction by 90 degrees so that:

$$\mathbf{R}(\frac{\pi}{2}, \vec{k}) \cdot \vec{U}_{rel} = \frac{\partial y(\bar{Z}, t)}{\partial t}\vec{\imath} + \Big(U - \frac{\partial x(\bar{Z}, t)}{\partial t}\Big)\vec{\jmath}. \tag{9}$$

To approximate the fluid forces, two wake coefficients, w and q are introduced and they are defined in the following way:

$$w = \frac{2C_D}{C_{D0}}, \quad q = \frac{2C_L}{C_{L0}}, \tag{10}$$

where C_{L0} is the initial lift coefficient. As proposed earlier, these wake coefficients are calculated using empirical wake oscillator equations which are designed in the way they can generate a self-excited and self-limited cycle oscillations of the fluid variables w and q, which represent the fluctuations of the drag and lift force. Following the approach taken in [25], the in-line oscillator will have frequency doubling coefficients.

Following [46], the model investigated in this study will be initially derived using two Van der Pol oscillators for fluctuations of the fluid forces presented by wake coefficients w and q:

$$\ddot{w} + 2\varepsilon_x \Omega_F (w^2 - 1)\dot{w} + 4\Omega_F^2 w = A_x \ddot{x};$$
$$\ddot{q} + \varepsilon_y \Omega_F (q^2 - 1)\dot{q} + \Omega_F^2 q = A_y \ddot{x}.$$

Here, ε_x and ε_y are fluid damping (Van der Pol) parameters, A_x and A_y are coupling coefficients, and Ω_F is the frequency of vortex shedding, dependent on the Strouhal number St:

$$\Omega_F = 2\pi St \frac{U}{D}. \tag{11}$$

Then the fluid force projections on the axes $\overline{X}$ and $\overline{Y}$ are calculated as:

$$\begin{aligned}(\vec{F}_F)_X &= (\vec{F}_D)_X + (\vec{F}_L)_X = \frac{\rho_F D}{4}\sqrt{\Big(U - \frac{\partial x}{\partial t}\Big)^2 + \Big(\frac{\partial y}{\partial t}\Big)^2}\Big(2C_{D0}U - \\ &- 2C_{D0}\frac{\partial x(\bar{Z}, t)}{\partial t} + w(\bar{Z}, t)C_{D0}^{fl}U - w(\bar{Z}, t)C_{D0}^{fl}\frac{\partial x(\bar{Z}, t)}{\partial t} + q(\bar{Z}, t)C_{L0}\frac{\partial y(\bar{Z}, t)}{\partial t}\Big);\end{aligned} \tag{12}$$

and

$$\begin{aligned}(\vec{F}_F)_Y &= (\vec{F}_D)_Y + (\vec{F}_L)_Y = \frac{\rho_F D}{4}\sqrt{\Big(U - \frac{\partial x}{\partial t}\Big)^2 + \Big(\frac{\partial y}{\partial t}\Big)^2}\Big(-2C_{D0}\frac{\partial y(\bar{Z}, t)}{\partial t} - \\ &- w(\bar{Z}, t)C_{D0}^{fl}\frac{\partial y(\bar{Z}, t)}{\partial t} + q(\bar{Z}, t)C_{L0}U - q(\bar{Z}, t)C_{L0}\frac{\partial x(\bar{Z}, t)}{\partial t}\Big).\end{aligned} \tag{13}$$

In order to integrate the model using a multi-mode approximation in the future, the expression $|\vec{U}_{rel}| = \sqrt{(U - \frac{\partial x}{\partial t})^2 + (\frac{\partial y}{\partial t})^2}$ needs to be expanded in a Taylor series. In the previous studies, Postnikov [50] has compared the responses of wake oscillator models which contain exact and approximate (where the terms of the third order and higher were neglected) expressions of the relative velocity $|\vec{U}_{rel}|$ in the formula for the fluid forces. He has shown that in the considered range of velocities there were no significant differences between the models behaviour. Therefore, in the current work only the terms up to the second order will be utilised as:

$$\sqrt{\Big(U - \frac{\partial x(\bar{Z}, t)}{\partial t}\Big)^2 + \Big(\frac{\partial y(\bar{Z}, t)}{\partial t}\Big)^2} = U\Big[1 - \frac{1}{U}\frac{\partial x(\bar{Z}, t)}{\partial t} + \frac{1}{2U^2}\Big(\frac{\partial y(\bar{Z}, t)}{\partial t}\Big)^2 + ...\Big]. \tag{14}$$

Finally, the complete dimensional system of equations for the two-dimensional structure is written as:

$$\begin{aligned}
m_*\ddot{x} &+ EIx'''' - T_b x'' - W_w\bar{Z}x'' - W_w x' = \frac{\rho_F D}{4}\Big(2C_{D0}U^2 - 4C_{D0}\dot{x}U + \\
&+ wC_{D0}^{fl}U^2 - 2wC_{D0}^{fl}\dot{x}U + qC_{L0}\dot{y}U + 2C_{D0}\dot{x}^2 + wC_{D0}^{fl}\dot{x}^2 - qC_{L0}\dot{x}\dot{y} + C_{D0}\dot{y}^2\Big), \\
m_*\ddot{y} &+ EIy'''' - T_b y'' - W_w\bar{Z}y'' - W_w y' = \frac{\rho_F D}{4}\Big(- 2C_{D0}U\dot{y} - C_{D0}^{fl}Uw\dot{y} + \\
&+ C_{L0}U^2 q - 2C_{L0}Uq\dot{x} + 2C_{D0}\dot{x}\dot{y}\Big), \\
\ddot{w} &+ 2\varepsilon_x\Omega_F(w^2-1)\dot{w} + 4\Omega_F^2 w = A_x\ddot{x}, \\
\ddot{q} &+ \varepsilon_y\Omega_F(q^2-1)\dot{q} + \Omega_F^2 q = A_y\ddot{y}.
\end{aligned} \tag{15}$$

The system of the equations (15) was transformed into a non-dimensional form using the following set of variables and parameters:

$$\tau = \omega_0 t, \quad X = \frac{x}{D}, \quad Y = \frac{y}{D}, \quad \omega_{ni} = \frac{\omega_{sti}}{\omega_0}, \quad \Omega_R = \frac{\Omega_F}{\omega_0}, \quad \zeta = \frac{\bar{Z}}{L}. \tag{16}$$

Here, τ, X, Y, ω_{ni}, Ω_R are dimensionless time, in-line displacement, cross-flow displacement, natural frequency of the mode number i, and vortex shedding frequency; ω_{sti} is the dimensional frequency of the mode i; ω_0 is the reference frequency; ζ is the non-dimensional coordinate indicating location along the beam; $\bar{Z}$ is the distance from the beginning of beam to the considered point; L is length of the beam.

The natural frequency of the horizontal beam of the mode i is:

$$\omega_{sti} = \frac{\pi i}{L}\sqrt{\frac{EI\pi^2 i^2}{L^2 m_*} + \frac{T_b}{m_*}}. \tag{17}$$

The full non-dimensional set of equations is as follows:

$$\begin{aligned}
\ddot{X} &+ \frac{EI}{m_*\omega_0^2}X'''' - \frac{T_b}{m_*\omega_0^2}X'' - \frac{W_w L\zeta}{m_*\omega_0^2}X'' - \frac{W_w}{m_*\omega_0^2}X' = \frac{a\Omega_R^2}{2\pi St} - \\
&- 2a\Omega_R\dot{X} + \frac{b\Omega_R^2}{4\pi St}w - b\Omega_R w\dot{X} + \frac{c\Omega_R}{2}q\dot{Y} + 2\pi Sta\dot{X}\dot{X} + \pi Sta\dot{Y}\dot{Y}, \\
\ddot{Y} &+ \frac{EI}{m_*\omega_0^2}Y'''' - \frac{T_b}{m_*\omega_0^2}Y'' - \frac{W_w L\zeta}{m_*\omega_0^2}Y'' - \frac{W_w}{m_*\omega_0^2}Y' = -a\Omega_R\dot{Y} - \frac{b}{2}\Omega_R w\dot{Y} + \\
&+ \frac{c\Omega_R^2}{4\pi St}q - c\Omega_R q\dot{X} + 2\pi Sta\dot{X}\dot{Y}, \\
\ddot{w} &+ 2\varepsilon_x\Omega_R w^2\dot{w} - 2\varepsilon_x\Omega_R\dot{w} + 4\Omega_R^2 w = A_x\ddot{X}, \\
\ddot{q} &+ \varepsilon_y\Omega_R q^2\dot{q} - \varepsilon_y\Omega_R\dot{q} + \Omega_R^2 q = A_y\ddot{Y},
\end{aligned} \tag{18}$$

where a, b and c are dimensionless coefficients:

$$a = \frac{C_{D0}\rho_F D^2}{4\pi m_* St}, \quad b = \frac{C_{D0}^{fl}\rho_F D^2}{4\pi m_* St}, \quad c = \frac{C_{L0}\rho_F D^2}{4\pi m_* St}. \tag{19}$$

The approximate solution is obtained using the Galerkin approximation, as in [46, 47], in the following form:

$$\begin{aligned}
X(\zeta,\tau) &= \sum_{n=1}^{N} X_n(\tau)\tilde{X}_n(\zeta), \quad Y(\zeta,\tau) = \sum_{i=1}^{N} Y_n(\tau)\tilde{Y}_n(\zeta), \\
w(\zeta,\tau) &= \sum_{n=1}^{N} w_n(\tau)\tilde{w}_n(\zeta), \quad q(\zeta,\tau) = \sum_{i=1}^{N} q_n(\tau)\tilde{q}_n(\zeta).
\end{aligned} \tag{20}$$

Here, sinusoidal functions are chosen as the mode shapes as $\tilde{X}_n(\zeta) = \tilde{Y}_n(\zeta) = \tilde{w}_n(\zeta) = \tilde{q}_n(\zeta) = \sin(n\pi\zeta)$. To derive the final set of the model equations, approximations Eqs.(20) are substituted into Eq.(18). Then both parts of the obtained equations are multiplied by $\sin(i\pi\zeta)$ and integrated with respect to the coordinate ζ over

the length of the structure. Finally, the resulting equations are multiplied by 2 so that the following system of ordinary differential equations is obtained:

$$
\begin{aligned}
\ddot{X}_i &+ 2a\Omega_R\dot{X}_i + \omega_{ni}^2 X_i = \frac{W_w}{Lm_*\omega_0^2}\sum_{n=1}^{N} X_n\Phi_{ni} + \frac{a\Omega_R^2}{i\pi^2 St}(1-\cos(i\pi)) + \\
&+ \frac{b\Omega_R^2}{4\pi St}w_i - b\Omega_R\sum_{n=1}^{N}\sum_{m=1}^{N} w_n\dot{X}_m\Pi_{nmi} + \frac{c\Omega_R}{2}\sum_{n=1}^{N}\sum_{m=1}^{N} q_n\dot{Y}_m\Pi_{nmi} + \\
&+ 2\pi Sta\sum_{n=1}^{N}\sum_{m=1}^{N}\dot{X}_n\dot{X}_m\Pi_{nmi} + \pi Sta\sum_{n=1}^{N}\sum_{m=1}^{N}\dot{Y}_n\dot{Y}_m\Pi_{nmi}, \\
\ddot{Y}_i &+ a\Omega_R\dot{Y}_i + \omega_{ni}^2 Y_i = \frac{W_w}{Lm_*\omega_0^2}\sum_{n=1}^{N} Y_n\Phi_{ni} - \frac{b}{2}\Omega_R\sum_{n=1}^{N}\sum_{m=1}^{N} w_n\dot{Y}_m\Pi_{nmi} + \\
&+ \frac{c}{4\pi St}\Omega_R^2 q_i - c\Omega_R\sum_{n=1}^{N}\sum_{m=1}^{N} q_n\dot{X}_m\Pi_{nmi} + 2\pi Sta\sum_{n=1}^{N}\sum_{m=1}^{N}\dot{X}_n\dot{Y}_m\Pi_{nmi}, \\
\ddot{w}_i &+ 2\varepsilon_x\Omega_R\sum_{n=1}^{N}\sum_{m=1}^{N}\sum_{l=1}^{N}\Big(\dot{w_n}w_m w_l\Psi_{nmli}\Big) - 2\varepsilon_x\Omega_R\dot{w}_i + 4\Omega_R^2 w_i = A_x\ddot{X}_i, \\
\ddot{q}_i &+ \varepsilon_y\Omega_R\sum_{n=1}^{N}\sum_{m=1}^{N}\sum_{l=1}^{N}\Big(\dot{q_n}q_m q_l\Psi_{nmli}\Big) - \varepsilon_y\Omega_R\dot{q}_i + \Omega_R^2 q_i = A_y\ddot{Y}_i,
\end{aligned}
\tag{21}
$$

where Φ_{ni}, Π_{nmi} and Ψ_{nmli} are dimensionless coefficients obtained during the discretization procedure due to the mode interaction:

$$
\Phi_{ni} = 2\Big[\int_0^1\Big(n\pi\cos(n\pi\zeta)\sin(i\pi\zeta)\Big)d\zeta - \int_0^1\Big(\zeta n^2\pi^2\sin(n\pi\zeta)\sin(i\pi\zeta)\Big)d\zeta\Big], \tag{22}
$$

$$
\Pi_{nmi} = 2\int_0^1\Big(\sin(n\pi\zeta)\sin(m\pi\zeta)\sin(i\pi\zeta)\Big)d\zeta, \tag{23}
$$

$$
\Psi_{nmli} = 2\int_0^1\Big(\sin(n\pi\zeta)\sin(m\pi\zeta)\sin(l\pi\zeta)\sin(i\pi\zeta)\Big)d\zeta. \tag{24}
$$

Thus, the system of equations (21) can be solved taking into account N modes containing $4N$ equations.

It should be noted that the coefficients Φ_{ni} and Ψ_{nmli} remain the same as derived in the model of flexible structure describing cross-flow vibrations only [46]. The term containing the coefficients Π_{nmi} is new and it accounts for mode interactions due to the in-line motion.

In order to explore different description of the fluid forces, the flexible model Eqs.(18) was modified where various nonlinear wake oscillators were used instead of the two original Van der Pol equations. These fluid oscillators are listed in Tables 1 and 2, and the nonlinear damping terms here have the following distinctions: (i) the same $(\varepsilon_x, \varepsilon_y)$ or different $(\varepsilon_{x1}, \varepsilon_{x2}, \varepsilon_{y1}, \varepsilon_{y2})$ fluid damping coefficients, (ii) number of damping terms (2 or 3 per oscillator), and (iii) contribution of the wake coefficient and its rate of change within the 3rd or 5th order terms. Combinations of oscillators allow managing the accuracy of prediction of the proposed model, and they are given in Table 3. Overall, 28 combinations of alternative oscillators are considered similar to the procedure in [5].

In Tables 1 and 2, the dimensionless coefficient Υ_{nmlksi} for the Landl equation is calculated using the following integral:

$$
\Upsilon_{nmlksi} = 2\int_0^1(\sin(n\pi\zeta)\sin(m\pi\zeta)\sin(l\pi\zeta)\sin(k\pi\zeta)\sin(s\pi\zeta)\sin(i\pi\zeta))d\zeta. \tag{25}
$$

Table 1: Different discretized in-line wake oscillators for two-dimensional flexible structure.

Oscillator	**Equation of motion**

Van der Pol	$\ddot{w}_i - 2\varepsilon_x\Omega_R\dot{w}_i + 2\varepsilon_x\Omega_R\sum_{n=1}^{N}\sum_{m=1}^{N}\sum_{l=1}^{N}\left(\dot{w}_n w_m w_l \Psi_{nmli}\right) + 4\Omega_R^2 w_i = A_x\ddot{X}_i;$
Modified Van der Pol	$\ddot{w}_i - 2\varepsilon_{x1}\Omega_R\dot{w}_i + 2\varepsilon_{x2}\Omega_R\sum_{n=1}^{N}\sum_{m=1}^{N}\sum_{l=1}^{N}\left(\dot{w}_n w_m w_l \Psi_{nmli}\right) + 4\Omega_R^2 w_i = A_x\ddot{X}_i;$
Rayleigh	$\ddot{w}_i - 2\varepsilon_x\Omega_R\dot{w}_i + 2\frac{\varepsilon_x}{\Omega_R}\sum_{n=1}^{N}\sum_{m=1}^{N}\sum_{l=1}^{N}\left(\dot{w}_n \dot{w}_m \dot{w}_l \Psi_{nmli}\right) + 4\Omega_R^2 w_i = A_x\ddot{X}_i;$
Modified Rayleigh	$\ddot{w}_i - 2\varepsilon_{x1}\Omega_R\dot{w}_i + 2\frac{\varepsilon_{x2}}{\Omega_R}\sum_{n=1}^{N}\sum_{m=1}^{N}\sum_{l=1}^{N}\left(\dot{w}_n \dot{w}_m \dot{w}_l \Psi_{nmli}\right) + 4\Omega_R^2 w_i = A_x\ddot{X}_i;$
Landl	$\ddot{w}_i + 2\varepsilon_{x1}\Omega_R\dot{w}_i - 2\varepsilon_x\Omega_R\sum_{n=1}^{N}\sum_{m=1}^{N}\sum_{l=1}^{N}\left(\dot{w}_n w_m w_l \Psi_{nmli}\right) +$ $+2\varepsilon_{x3}\Omega_R\sum_{n=1}^{N}\sum_{m=1}^{N}\sum_{l=1}^{N}\sum_{k=1}^{N}\sum_{s=1}^{N}\left(\dot{w}_n w_m w_l w_k w_s \Upsilon_{nmlksi}\right) + 4\Omega_R^2 w_i = A_x\ddot{X}_i;$
Krenk-Nielsen	$\ddot{w}_i - 2\varepsilon_{x1}\Omega_R\dot{w}_i + 2\varepsilon_{x2}\Omega_R\sum_{n=1}^{N}\sum_{m=1}^{N}\sum_{l=1}^{N}\left(\dot{w}_n w_m w_l \Psi_{nmli}\right) +$ $+2\frac{\varepsilon_{x3}}{\Omega_R}\sum_{n=1}^{N}\sum_{m=1}^{N}\sum_{l=1}^{N}\left(\dot{w}_n \dot{w}_m \dot{w}_l \Psi_{nmli}\right) + 4\Omega_R^2 w_i = A_x\ddot{X}_i;$

Table 2: Different discretized cross-flow wake oscillators for two-dimensional flexible structure.

Oscillator	**Equation**
Van der Pol	$\ddot{q}_i - \varepsilon_y\Omega_R\dot{q}_i + \varepsilon_y\Omega_R\sum_{n=1}^{N}\sum_{m=1}^{N}\sum_{l=1}^{N}\left(\dot{q}_n q_m q_l \Psi_{nmli}\right) + \Omega_R^2 q_i = A_y\ddot{Y}_i;$
Modified Van der Pol	$\ddot{q}_i - \varepsilon_{y1}\Omega_R\dot{q}_i + \varepsilon_{y2}\Omega_R\sum_{n=1}^{N}\sum_{m=1}^{N}\sum_{l=1}^{N}\left(\dot{q}_n q_m q_l \Psi_{nmli}\right) + \Omega_R^2 q_i = A_y\ddot{Y}_i;$
Rayleigh	$\ddot{q}_i - \varepsilon_y\Omega_R\dot{q}_i + \frac{\varepsilon_y}{\Omega_R}\sum_{n=1}^{N}\sum_{m=1}^{N}\sum_{l=1}^{N}\left(\dot{q}_n \dot{q}_m \dot{q}_l \Psi_{nmli}\right) + \Omega_R^2 q_i = A_y\ddot{Y}_i;$
Modified Rayleigh	$\ddot{q}_i - \varepsilon_{y1}\Omega_R\dot{q}_i + \frac{\varepsilon_{y2}}{\Omega_R}\sum_{n=1}^{N}\sum_{m=1}^{N}\sum_{l=1}^{N}\left(\dot{q}_n \dot{q}_m \dot{q}_l \Psi_{nmli}\right) + \Omega_R^2 q_i = A_y\ddot{Y}_i;$

Landl	$$\ddot{q}_i + \varepsilon_{y1}\Omega_R\dot{q}_i - \varepsilon_{y2}\Omega_R \sum_{n=1}^{N}\sum_{m=1}^{N}\sum_{l=1}^{N}\left(\dot{q}_n q_m q_l \Psi_{nmli}\right) + \\ + \varepsilon_{y3}\Omega_R \sum_{n=1}^{N}\sum_{m=1}^{N}\sum_{l=1}^{N}\sum_{k=1}^{N}\sum_{s=1}^{N}\left(\dot{q}_n q_m q_l q_k q_s \Upsilon_{nmlksi}\right) + \Omega_R^2 q_i = A_y \ddot{Y}_i;$$
Krenk-Nielsen	$$\ddot{q}_i - \varepsilon_{y1}\Omega_R\dot{q}_i + \varepsilon_{y2}\Omega_R \sum_{n=1}^{N}\sum_{m=1}^{N}\sum_{l=1}^{N}\left(\dot{q}_n q_m q_l \Psi_{nmli}\right) + \\ + \frac{\varepsilon_{y3}}{\Omega_R} \sum_{n=1}^{N}\sum_{m=1}^{N}\sum_{l=1}^{N}\left(\dot{q}_n \dot{q}_m \dot{q}_l \Psi_{nmli}\right) + \Omega_R^2 q_i = A_y \ddot{Y}_i;$$

Table 3: Investigated combinations of oscillators ("✓" denotes the combinations covered in this research, and "-" means the combination is not covered).

Cross-flow / **In-line**	Van der Pol	Modified Van der Pol	Rayleigh	Modified Rayleigh	Landl	Krenk-Nielsen
Van der Pol	✓	-	✓	-	✓	✓
Modified Van der Pol	-	✓	-	✓	✓	✓
Rayleigh	✓	-	✓	-	✓	✓
Modified Rayleigh	-	✓	-	✓	✓	✓
Landl	✓	✓	✓	✓	✓	✓
Krenk-Nielsen	✓	✓	✓	✓	✓	✓

The next section provides the summary of the calibration procedure, description of experimental data selected for calibration, the short-list of the calibrated models with appropriate sets of coefficients and the comparison of the presented options.

3 Calibration results

As all wake oscillator models are inherently empirical, they require careful selection/calibration of the empirical parameters based on the experimental data. In the current work, displacement amplitudes of a flexible structure in uniform flow are chosen for model calibration and the experimental results by Sanaati and Kato [48] are used. In [48] a flexible beam is positioned horizontally, and different cases of axial stiffness are considered. The first case implies no axial vibrations, while the structure oscillates in both in-line and cross-flow directions.

The data presented in [48] contains only the cross-flow displacement, but nevertheless the structure had the capacity to move in both cross-flow and in-line directions. The data set consists of 25 data points in the range of reduced velocity from 1.8 to 15.0, corresponding to a velocity of the flow from 0.10 to 0.82 m/s and the Reynolds number from 1780 to 14800 approximately. The maximum non-dimensional displacement is 0.48 recorded at the reduced velocity of 5.7. The mass ratio reported in [48] is 1.17 which corresponds to mass-damping ratios $\mu\xi = 0.0281$ and $(\mu + C_A)\xi = 0.0521$ (if $C_A = 1$). The considered flexible beam has the length of 2.92 m, diameter of 0.018 m, applied tension of 147 N and bending stiffness of 9.0 Nm^2. The displacement

measurements in [48] were performed at the cross-section of $\zeta = 0.5$ (middle of the beam), therefore, all versions of the model are calibrated for this cross-section. The reduced velocity from the experimental data available in the literature is used in all calculations performed in this paper, which is defined by using the experimentally determined frequency of the first mode ω_{st1} as $U_R = \frac{U}{\omega_{st1} D}$.

Calibration is performed by using the schemes which are very similar to the ones utilised in the case of the 2DOF rigid structure in [5]. Experimental data by Sanaati and Kato [48] are obtained using the standard deviation of the recorded displacement signal, and therefore only the algorithms with the standard deviation are applied for calibration. Calibration scheme "Cross-flow 1" computes the objective function using the weighted sum of the absolute squared differences, and the scheme "Cross-flow 2" - using the weighted sum of the relative errors in each of the control points. All 28 versions of the new flexible model are the subject to calibration, as performed for the rigid structure model in [5]. In these versions, the wake oscillator equations given in Tables 1 and 2 are applied in pairs. Calibration is performed for only a 1 mode approximation of the model of a flexible structure.

The most accurate models obtained during the calibration procedure are listed in Table 4 from the best option at the top to the least accurate option in the bottom. The quality of the fit provided by the identified options is illustrated in Fig. 2, where a comparison of the experimental results and the model predictions in terms of amplitudes of the in-line and cross-flow displacements is shown for different reduced velocities. Table 4 presents the accuracy rating for considered models only in terms of the cross-flow displacement.

Table 4: The most accurate models calibrated using data by Sanaati and Kato [48].

Option	Fluid nonlinearities	Scheme	Set of coefficients
1	Krenk-Nielsen - Van der Pol	Cross-flow 2	$C_{L0} = 0.33, C_{D0} = 1.37, C_{D0}^{fl} = 1.06, \varepsilon_{x1} = 0.8990, \varepsilon_{x2} = 1.6158, \varepsilon_{x3} = 2.5295, \varepsilon_y = 0.0895, A_x = 10.88, A_y = 6.51, C_A = 1.00, K = 0.57$
2	Van der Pol - Van der Pol	Cross-flow 2	$C_{L0} = 0.74, C_{D0} = 1.59, C_{D0}^{fl} = 0.01, \varepsilon_x = 0.8154, \varepsilon_y = 1.0116, A_x = 11.96, A_y = 3.94, C_A = 2.77, K = 1.35$
3	Rayleigh - Rayleigh	Cross-flow 1	$C_{L0} = 0.72, C_{D0} = 2.60, C_{D0}^{fl} = 1.55, \varepsilon_x = 0.7041, \varepsilon_y = 0.0825, A_x = 12.37, A_y = 8.43, C_A = 2.15, K = 0.88$
4	Modified Rayleigh - Krenk-Nielsen	Cross-flow 2	$C_{L0} = 0.49, C_{D0} = 2.36, C_{D0}^{fl} = 1.61, \varepsilon_{x1} = 0.8687, \varepsilon_{x2} = 0.4177, \varepsilon_{y1} = 0.6427, \varepsilon_{y2} = 0.0900, \varepsilon_{y3} = 0.0312, A_x = 12.06, A_y = 11.07, C_A = 3.23, K = 1.67$
5	Modified Rayleigh - Modified Van der Pol	Cross-flow 2	$C_{L0} = 0.29, C_{D0} = 1.74, C_{D0}^{fl} = 0.19, \varepsilon_{x1} = 0.3028, \varepsilon_{x2} = 0.3498, \varepsilon_{y1} = 0.0645, \varepsilon_{y2} = 0.0478, A_x = 11.98, A_y = 11.90, C_A = 1.17, K = 0.47$
6	Landl - Krenk-Nielsen	Cross-flow 2	$C_{L0} = 0.44, C_{D0} = 1.68, C_{D0}^{fl} = 0.21, \varepsilon_{x1} = 0.3050, \varepsilon_{x2} = 0.3131, \varepsilon_{x3} = 0.3092, \varepsilon_{y1} = 0.0614, \varepsilon_{y2} = 0.0604, \varepsilon_{y3} = 0.0538, A_x = 12.00, A_y = 12.00, C_A = 1.48, K = 0.25$

It should be noted that the applicability boundaries for the identified sets of coefficients have to be carefully checked in the future. Our results indicate that these coefficients vary significantly depending on the structural configuration, mass ratio, damping ratio and Reynolds number range. The quality of the fit for the target experimental data varies as follows:

- Option 1 of Table 4 (Krenk-Nielsen - Van der Pol system), shown in dark blue in Fig. 2, provides an almost exact fit of the transition from the initial branch to the super-upper branch for the cross-flow

displacement. An overestimation is visible for the region of reduced velocity from approximately 6 to 8, and underestimation in the region of reduced velocity from 8 to 12. This Option also predicts two resonance peaks of the in-line displacement amplitude with the first peak greater than the second one.

- Option 2 of Table 4 (Van der Pol - Van der Pol system), shown in red in Fig. 2, demonstrates the growing branch of the cross-flow resonance peak very similar to Option 1. The cross-flow lower branch is not properly described by this model as it demonstrates significant underestimation of the displacement amplitude for this region ($U_R \in (8.0, 12.0)$). In the in-line direction, Option 2 shows one resonance peak at the reduced velocity of 5, which is significantly lower than the other models predict.

- Option 3 of Table 4 (Rayleigh - Rayleigh system), shown in yellow in Fig. 2, gives the peak predictions for both directions qualitatively very similar to Option 1. In the cross-flow direction, Option 3 demonstrates higher error with the experimental data. In the in-line direction, the first resonance is higher than the second resonance, and the displacement amplitudes are higher than predicted by Option 1.

- Option 4 of Table 4 (Modified Rayleigh - Krenk-Nielsen system), shown in violet in Fig. 2, shows the best agreement with the experimental data of the cross-flow displacement until the reduced velocity of 7.0. Prediction of the initial branch up to the reduced velocity of 5.1 is quite consistent with the prediction by Options 1 and 2. Option 6 predicts an earlier and higher cross-flow peak value in the interval ($U_R \in (5.1, 5.7)$) in between the available experimental data points, and the interval of the reduced velocity from 5.7 to 6.8 is estimated significantly better than by the other models with the lowest errors. For the reduced velocity higher than 7.0, the cross-flow lower branch is significantly underestimated. In the in-line direction, Option 4 predicts the highest first resonance peak among the models, but relatively average second resonance peak.

- Option 5 of Table 4 (Modified Rayleigh - Modified Van der Pol system), shown in green in Fig. 2, agrees well with the prediction given in Option 3 in terms of the cross-flow displacement. In the in-line direction, Option 5 has a much better agreement with Option 6 which implies a very small first synchronisation peak and a big second peak.

- Option 6 of Table 4 (Landl - Krenk-Nielsen system), shown in blue in Fig. 2, demonstrates a wider version of the cross-flow resonance peak: overestimated initial branch and the region ($U_R \in (6.0, 8.0)$). The in-line lock-in develops with the second peak only.

Thus, the main differences among the considered options are focused around the width of the initial and super-upper branches in terms of the reduced velocity range and the balance between the in-line lock-in peaks. For in-line direction, three out of six considered models predict the amplitudes during the first synchronisation to be greater than the second synchronisation; two options predict the first peak to be much lower than the second peak and the last option shows that the first peak is not present or negligible.

If only the accuracy of predicting the cross-flow displacement is taken into account, the models collected in Table 4 show that both Rayleigh and Van der Pol damping terms are applicable for VIV prediction for this combination of case parameters. Option 1 of Table 4 (Krenk-Nielsen - Van der Pol system calibrated with the scheme Cross-flow 2) gives the most accurate prediction of the cross-flow displacement observed in the experiments by Sanaati and Kato [48] in accordance with the previously formulated objective function. The properties of this model are analysed in the next Section.

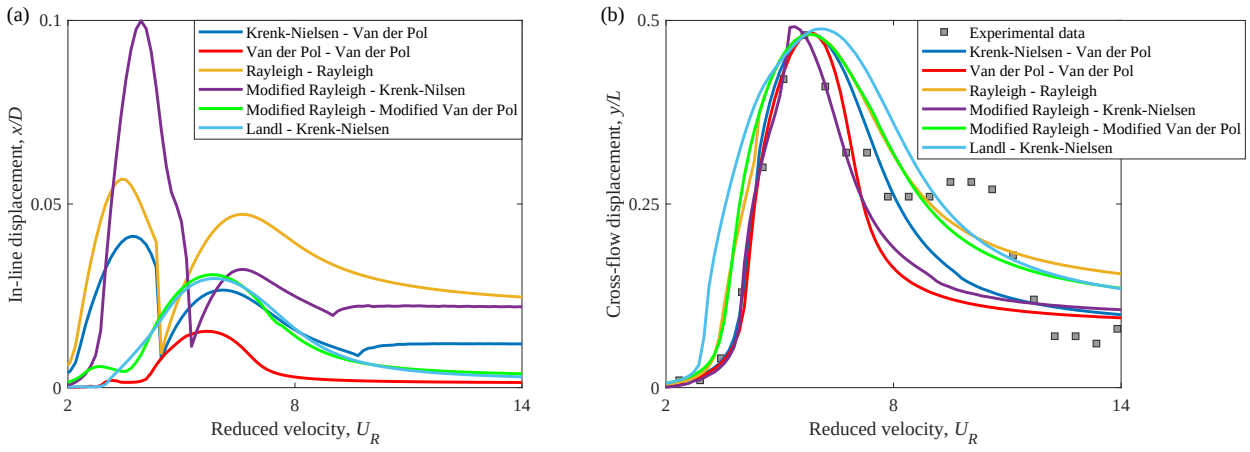

Figure 2: Displacement amplitudes during synchronisation state over the range of reduced velocity of the flow U_R predicted by the models from Table 4 calibrated in respect to the experimental data [48]: (a) prediction of in-line amplitudes of displacement; (b) calibrated cross-flow amplitudes of displacement. Mass ratio is $\mu = 1.17$, damping ratio is $\xi = 0.024$, Reynolds number range from 1780 to 14800.

4 Krenk-Nielsen - Van der Pol model

The dynamic responses of a horizontal beam have been analysed using calibrated Krenk-Nielsen - Van der Pol model for a range of vortex shedding frequency or related reduced velocity. The reduced velocity was calculated based on the first natural frequency of the beam. As this work is primarily focused on the in-line and cross-flow displacements $X(\tau, \zeta)$ and $Y(\tau, \zeta)$, the behaviour of the wake coefficients w and q and corresponding fluid forces will not be shown in this paper. Three and five mode approximations were calculated (i.e. $X(\zeta, \tau) = \sum_{n=1}^{N} X_n(\tau)\tilde{X}_n(\zeta)$ and $Y(\zeta, \tau) = \sum_{i=1}^{N} Y_n(\tau)\tilde{Y}_n(\zeta)$ for $N = 3$ and 5), and this section provides details of the obtained solutions for $X_n(\tau)$ and $Y_n(\tau)$. The following analysis of the model dynamics is given only for the option with Krenk-Nielsen - Van der Pol damping which appears to be the most accurate calibration result, but it is possible to extend it to further options in the future.

4.1 Five mode approximation

The calibrated model with Krenk-Nielsen - Van der Pol damping can account for different numbers of modes. Displacement amplitudes at different positions along the beam predicted by a 5 mode approximation of the model are given in Fig. 3 for the cross-flow and in-line directions. They were calculated for a range of reduced velocity and are presented here as function of vortex shedding frequency, Ω_R. The values in these figures are the standard deviations of the displacement signals obtained using Eq. (18).

The results displayed in Figs 3a, 3b, 3e and 3f are qualitatively consistent with the ones shown in [46] for a one-dimensional system, where the structure oscillates in the cross-flow direction only. The cross-flow displacement amplitudes at the cross-section $\zeta = 0.10$ in Fig. 3a show the growth in amplitude from the first lock-in peak to the fifth lock-in peak. The cross-section $\zeta = 0.50$ in Fig. 3b corresponds to a practical absence of the second and forth resonance peaks, because of the nodal point of the second and the forth modes. The location $\zeta = 0.35$ is in proximity of the node of the third mode, which results in the absence of the third resonance peak in Fig. 3e. Finally, the location $\zeta = 0.75$ is the node of the forth mode, where the lock-in peak does not develop, as shown in Fig. 3f. The location $\zeta = 0.75$ is also an antinode for the second mode, which results in the highest second peak in the mentioned records.

The peak record taken for the in-line displacement shows much more consistency throughout the different

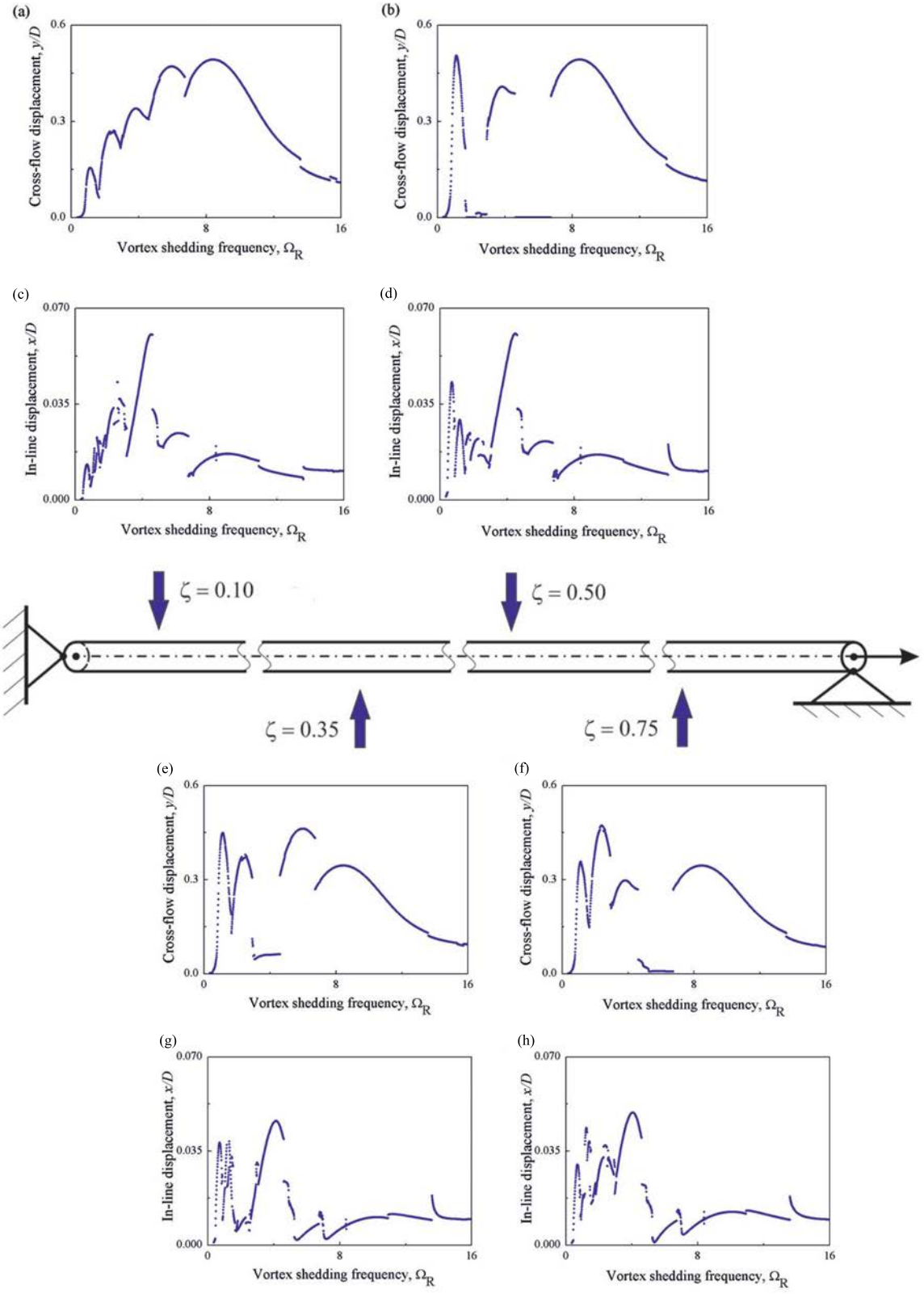

Figure 3: Displacement amplitudes at different locations along the horizontally positioned structure: (a) cross-slow amplitudes at $\zeta = 0.10$; (b) cross-slow amplitudes at $\zeta = 0.50$; (c) in-line amplitudes at $\zeta = 0.10$; (d) in-line amplitudes at $\zeta = 0.50$; (e) cross-slow amplitudes at $\zeta = 0.35$; (f) cross-slow amplitudes at $\zeta = 0.75$; (g) in-line amplitudes at $\zeta = 0.35$; (h) in-line amplitudes at $\zeta = 0.75$. The model is approximated for 5 modes.

locations in Figs 3c, 3d, 3g and 3h. The third resonance peak practically appears to be the highest for all considered locations, even near the nodal point of the third mode at $\zeta = 0.35$, as in Fig. 3g. Also, the peaks around the first and second resonance frequencies emerge not as two single peaks, but a combination of 2-4 peaks with unclear borders. The pattern of growth of peak heights at $\zeta = 0.10$, as in Fig. 3a, is present in Fig. 3c from the first couple of peaks to the third peak.

The location of the in-line nodal points can be the result of applying sinusoidal functions in modes approximation and, also, the frequency doubling coefficients in the wake equation. Hence, the question about introducing frequency doubling coefficients when considering multiple modes should be more thoroughly addressed in the future research, based on the experimental evidence on the development of in-line modes.

Fig. 4 shows the trajectories of the in-line and cross-flow displacements at the reduced velocities of 6.0, 10.0, 20.0, 28.0 and 45.0, which correspond to the peaks of cross-flow displacement amplitudes in Figs 3a, 3b, 3e and 3f in different cross-sections. It is possible to observe the variations of the "moon" shape throughout all the cross-sections at the $U_R = 10.0$ and $U_R = 45.0$. At the other reduced velocities, the transitions from the "figure-of-eight" to the "moon" shape are observed. The reversed "moon" shape is observed at $U_R = 20.0$ at the cross-sections $\zeta = 0.10$ and $\zeta = 0.50$ and at $U_R = 28.0$ and $U_R = 45.0$ at the cross-sections $\zeta = 0.25$ and $\zeta = 0.35$. The amplitude of oscillations reduces in the cross-flow direction when the cross-section is corresponding to the nodal points of separate modes or located near them. Thus, the cross-flow amplitudes of the second mode reduce at the cross-section $\zeta = 0.50$, cross-flow amplitudes of the third mode - at the cross-section $\zeta = 0.35$, and the forth mode cross-flow displacement decays at the cross-sections $\zeta = 0.25$ and $\zeta = 0.50$.

The dominating frequencies obtained by the 5 mode approximation of the model are presented in Fig. 5.

4.2 Co-existing solutions

Our analysis of the system dynamics reveals that co-existing solutions are observed at some reduced velocity ranges. To explore these phenomena, 3 mode approximation is considered and the results are presented in this section. To demonstrate these solutions, amplitudes of modal coefficients $X_1(\tau)$, $Y_1(\tau)$, $X_2(\tau)$, $Y_2(\tau)$, $X_3(\tau)$ and $Y_3(\tau)$ are displayed in Fig. 6 for the considered reduced velocity range. As can be seen from this figure, co-existing responses are observed around reduced velocities 7.8 to 8.8 and 14.1 to 15.3. In these both regions, three solutions are obtained depending on the initial conditions applied for integration.

It should be noted that in both cases the co-existing solutions are observed away from the resonance peaks near the locations of frequency lock-ins switches shown in Fig. 7 where the frequencies of in-line and cross-flow displacements at locations $\zeta = 0.25$, 0.35, 0.50 are presented. While at the top of the resonance peak solutions are mostly harmonic, these responses at the lock-in boundaries are complex, and the standard deviation although being computationally convenient, does not provide adequate information about them.

The time histories of the modal coefficients corresponding to different solutions at the reduced velocity $U_R = 8.2$ are shown in Figs 8, 9 and 10 by blue, green and violet colours corresponding to the solutions presented in Fig. 6. A set of figures showing co-existing solutions at the reduced velocity 14.6 (Figs 13 and 14) is included in Appendix A and the time histories in orange, violet and red in these figures correspond to the solutions in respective colours in Fig. 6.

The first feature that appears to be common for Figs 8, 9, 10 and 13 is that time histories are highly modulated, especially, for the in-line coefficients X_1, X_2, X_3. The highest amplitudes belong to the modal coefficients Y_1 and X_3 in Fig. 8, Y_1 and X_2 in Fig. 9, Y_2 and X_3 in Fig. 10, Y_3 and X_3 in Fig. 13, and they appear indeed to be less modulated than others.

There is also a similarity in displacement amplitudes observed in the green solution detailed in Fig. 9

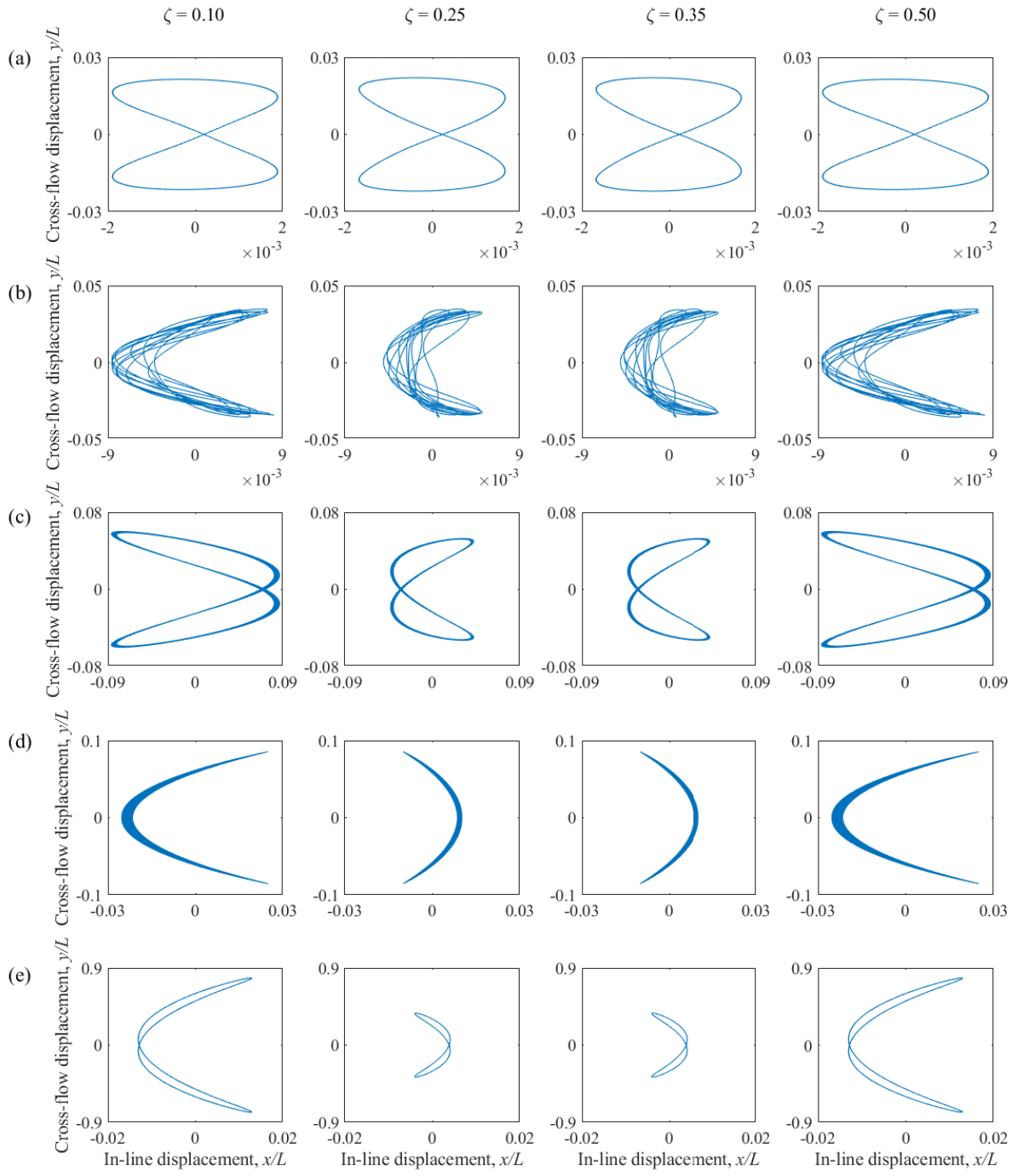

Figure 4: Displacement orbits generated by the 5 mode approximation at the locations $\zeta = 0.10, 0.25, 0.35$ and 0.50 for the following reduced velocities: (a) $U_R = 6.0$ corresponding to $\Omega_R = 1.2$; (b) $U_R = 10.0$ corresponding to $\Omega_R = 2.0$; (c) $U_R = 20.0$ corresponding to $\Omega_R = 4.0$; (d) $U_R = 28.0$ to $\Omega_R = 5.6$ and (e) $U_R = 45.0$ corresponding to $\Omega_R = 9.0$.

and in the solution marked in violet and shown in Fig. 10, where both are highly modulated in the in-line modal coefficients and provide similar values of the standard deviation. However, they have definitely different frequencies as can be seen from Fig. 7. Also, the solution marked in violet calculated for the reduced velocity of 8.20 is more computationally demanding.

Fig. 11 in this section and Fig. 15 in Appendix B show the co-existing solution orbits on the phase planes at the cross-sections $\zeta = 0.10$, 0.25, 0.35 and 0.50 calculated for the reduced velocities of 8.2 and 14.6. The

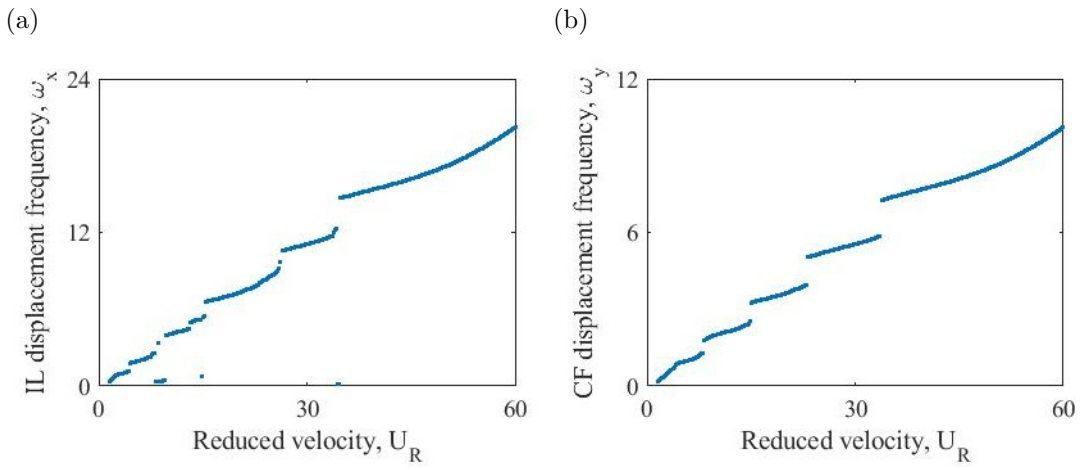

Figure 5: Dominating frequencies generated by the 5 mode approximation of the model for the cross-section $\zeta = 0.35$: (a) in-line displacement frequencies; (d) cross-flow displacement frequencies.

modulations observed above for the 3 modes approximation of the considered model result in drifting shapes from "figure-of-eight" to "moon" shape and back for all three solutions at the reduced velocity of 8.2, as displayed in Fig. 11. Orbits in Figs 15a and 15b are much more clear, even balancing between "figure-of-eight" and "moon" shapes, and relatively close to each other in terms of amplitudes at cross-sections $\zeta = 0.1$ and $\zeta = 0.25$. The orbits at peaks of the modal coefficient X_1 (shown in Fig. 6a) are displayed in Fig. 16 in Appendix B for $U_R = 3.6$, 6.0, 13.0 and 21.0.

In summary, the analysis conducted in this subsection confirms that modulation of the generated signals reduces with the amplitude growth. The most modulated signals belong to the in-line direction, and the first mode appears to be the best indicator of the solution switch. These results are obtained using simple modifications of initial conditions and can be improved if other techniques of search for coexisting solutions will be applied.

The next section discusses the differences of how the various combinations of oscillators perform in terms of the modal coefficients and final displacements over the range of the reduced velocity of the flow.

5 Comparison of models

This section compares the first three models from Table 4 containing Krenk-Nielsen - Van der Pol damping, Van der Pol - Van der Pol damping and Rayleigh - Rayleigh damping. The differences are demonstrated using 3 mode approximations in terms of the modal coefficients $X_1, X_2, X_3, Y_1, Y_2, Y_3$ and the final displacements X and Y over the range of the reduced velocity $U_R = \frac{U}{D\omega_{st1}}$, computed using the experimental frequency of the first mode ω_{st1} [48].

The modal coefficients X_1 and X_3 of the aforementioned models demonstrate an occurrence of multiple co-existing solutions as was discussed in the previous section of this paper. The modal coefficient X_1 contains at least four lock-in peaks of a variative height generated by all the considered models. Options 1 and 3 generate the first resonance peak in the modal coefficient X_1 as the highest, which can potentially come from the presence of the Rayleigh damping term in equation of the drag force fluctuations. The majority of the co-existing solutions are observed in the small intervals of reduced velocity that are located approximately from $U_R = 8.0$ to $U_R = 16.0$ for all the in-line coefficients X_1, X_2, X_3. The generated time histories are complex in this region, and the standard deviations are a very simplified representation of the generated dynamics. Model 3 generates the highest modal coefficients X_1, X_2, X_3 and the highest in-line displacement peaks as shown in

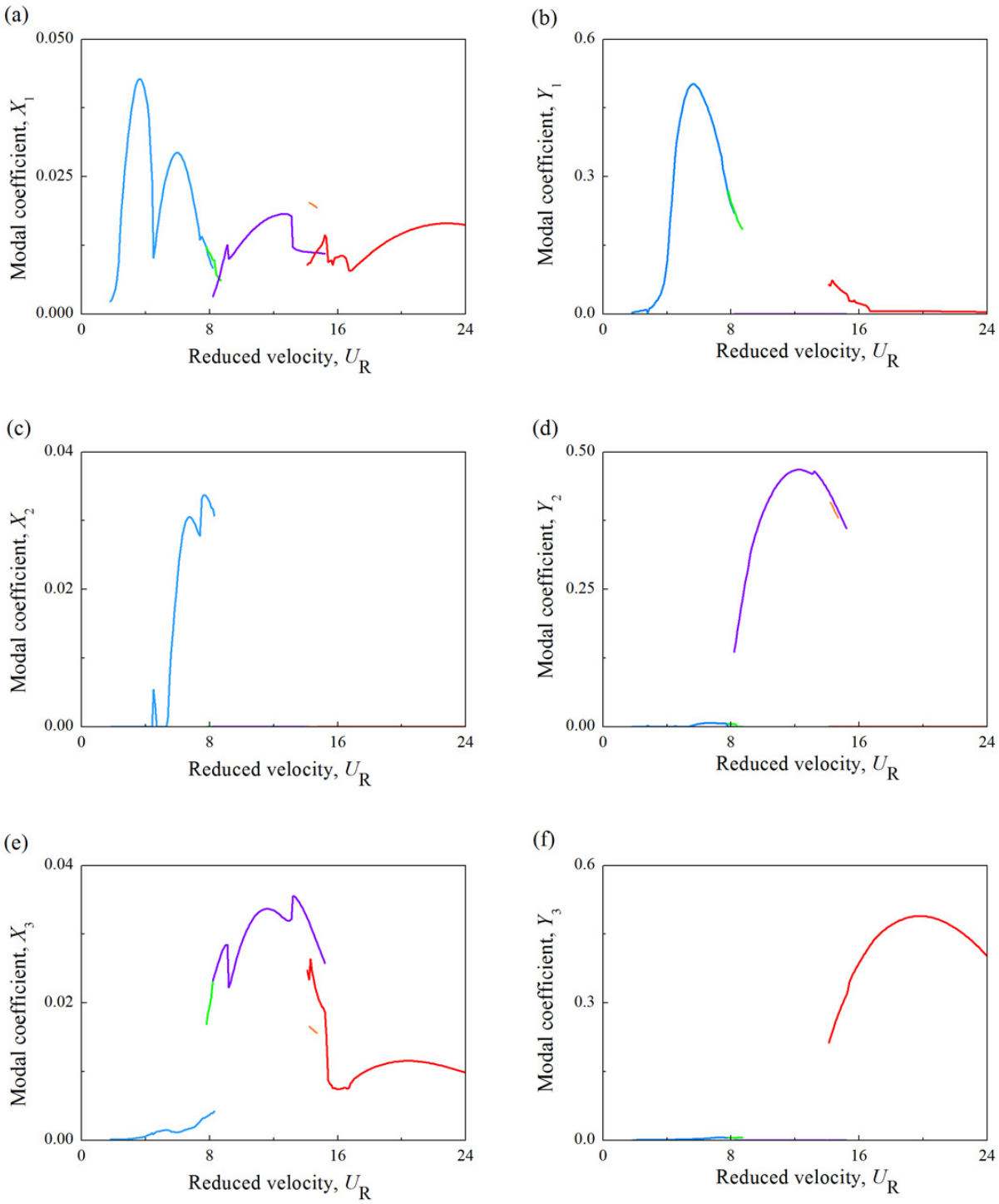

Figure 6: Amplitudes of the modal coefficients over the reduced velocity range generated by the 3 modes approximation of the model with Krenk-Nielsen - Van der Pol damping: (a) modal coefficient X_1; (b) modal coefficient Y_1; (c) modal coefficient X_2; (d) modal coefficient Y_2; (e) modal coefficient X_3; (f) modal coefficient Y_3. Blue, green, violet, orange and red lines denote five coexisting solutions.

Figs 12a, 12c, 12e and 12g. This model also indicates the presence of a relatively high in-line peak around the reduced velocity $U_R = 25$.

The contribution of the modal coefficients in the final displacement of the structure in the cross-flow directon varies with the cross-section considered, which leads to a different distribution of the peak heights in both directions. In Fig. 12b, the third lock-in peak around $U_R = 20$ is the highest, due to a significant contribution

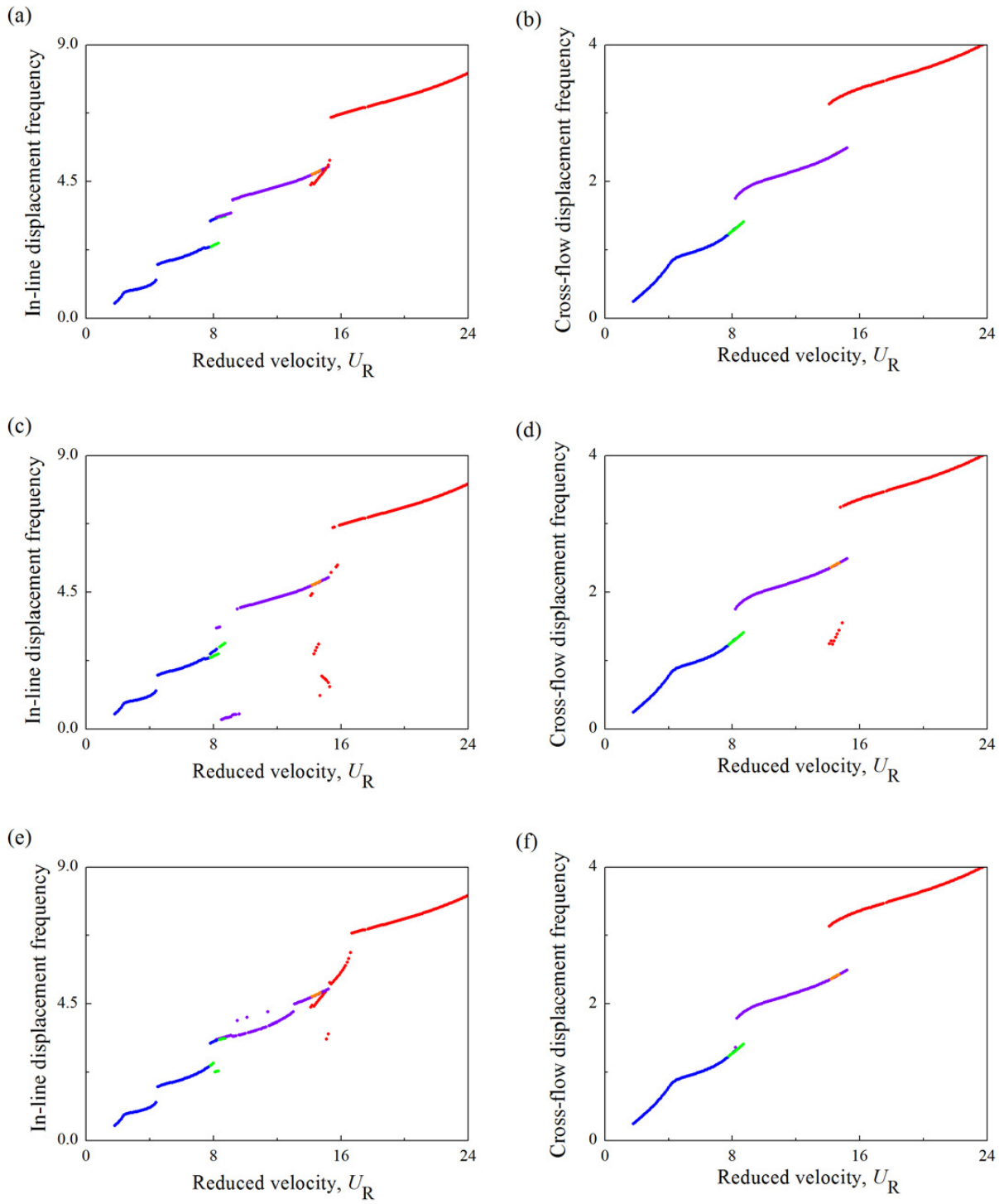

Figure 7: Frequencies of displacement signals at different locations generated by 3 modes approximation model: (a) frequencies of in-line displacement amplitudes at $\zeta = 0.25$; (b) frequencies of cross-flow displacement amplitudes at $\zeta = 0.25$; (c) frequencies of in-line displacement amplitudes at $\zeta = 0.35$; (d) frequencies of cross-flow displacement amplitudes at $\zeta = 0.35$; (e) frequencies of in-line displacement amplitudes at $\zeta = 0.50$; (f) frequencies of cross-flow displacement amplitudes at $\zeta = 0.50$.

of the third mode at $\zeta = 0.10$. The cross-section $\zeta = 0.25$ corresponds to the antinode of the second mode and results in the second highest peak around $U_R = 10$ in Fig. 12d. At the cross-sections $\zeta = 0.35$ and $\zeta = 0.50$, the displacement amplitudes demonstrate the highest first peak for almost all the considered models in Figs 12f and 12h. The cross-section $\zeta = 0.35$ is in the proximity of the nodal point of the third mode, this is why, the

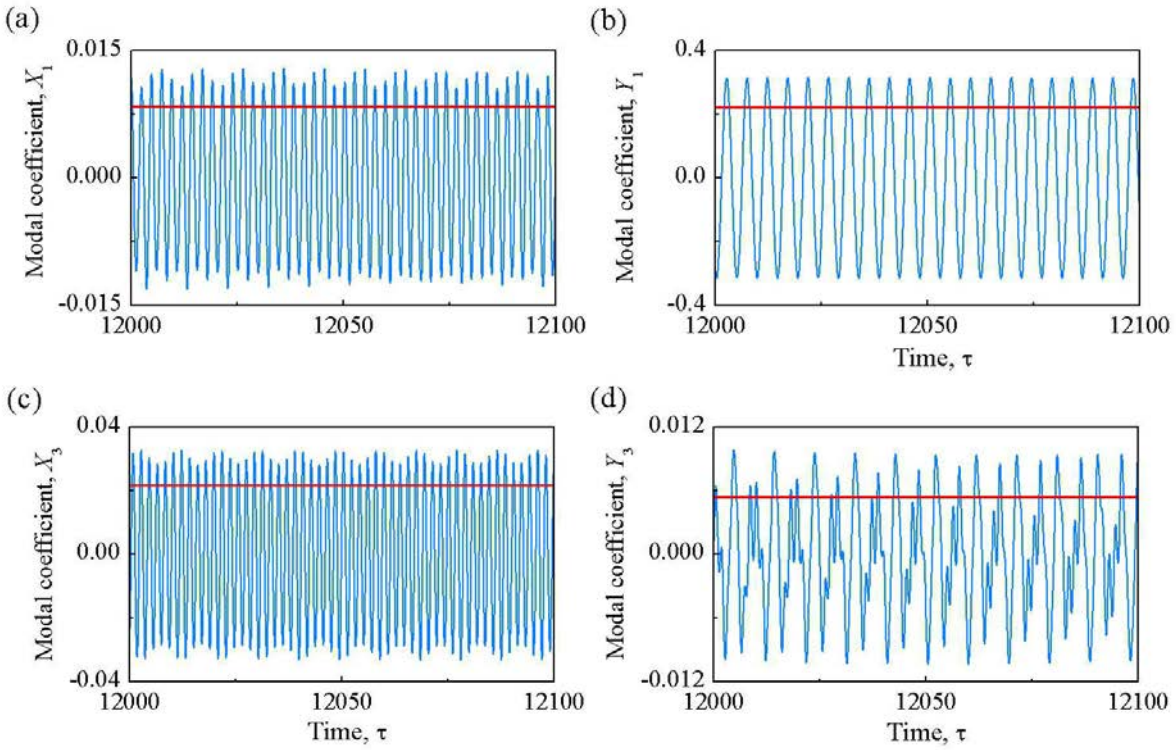

Figure 8: Time histories of amplitudes of the modal coefficients generated by the 3 modes approximation of the model with Krenk-Nielsen - Van der Pol damping at reduced velocity $U_R = 8.2$ corresponding to the blue solution in Fig. 6: (a) modal coefficient X_1; (b) modal coefficient Y_1; (c) modal coefficient X_3; (d) modal coefficient Y_3. Red line denotes the value of standard deviation of the signal. The modal coefficients X_2 and Y_2 have comparatively small values and are not presented in this figure.

third peak is practically absent in Fig. 12f. Respectively, the cross-section $\zeta = 0.50$ corresponds to the nodal point of the second mode, hence, Fig. 12h shows absence of the second resonance peak.

The in-line displacement in the range below $U_R = 15.0$ shows the similar peak patterns as in the cross-flow direction. In particular, responses of Models 1 and 3, depicted in Fig. 12a, show four peaks in this velocity interval with the fourth peak highest, and in Fig. 12c the second peak is the highest, although they occur earlier than in the cross-flow direction in terms of the reduced velocity range. In the cross-section $\zeta = 0.35$ in Fig. 12e, the first and the second peaks generated by these options are approximately of the same height. And in the cross-section $\zeta = 0.50$ in Fig. 12g, the first peak is the highest.

The in-line displacement in Fig. 12 in the range from approximately $U_R = 15.0$ to $U_R = 30.0$ shows a significant wide peak which is defined by the contribution of the modal coefficients X_1 and X_3. The peak shape is influenced mainly by the third harmonics in the cross-sections $\zeta = 0.10$ and $\zeta = 0.25$ (see Figs 12a and 12c), by the first harmonics only - in the cross-section $\zeta = 0.35$ (see Fig. 12e), and by both the first and the third harmonics - in the anti-nodal cross-section $\zeta = 0.50$ (see Fig. 12g). The in-line displacement suggested by Model 2 shows a less visible presence of co-existing solutions, less peaks and lower amplitudes, with the second peak highest in the cross-sections $\zeta = 0.10$ and $\zeta = 0.25$ and with the first peak highest in the cross-sections $\zeta = 0.35$ and $\zeta = 0.50$.

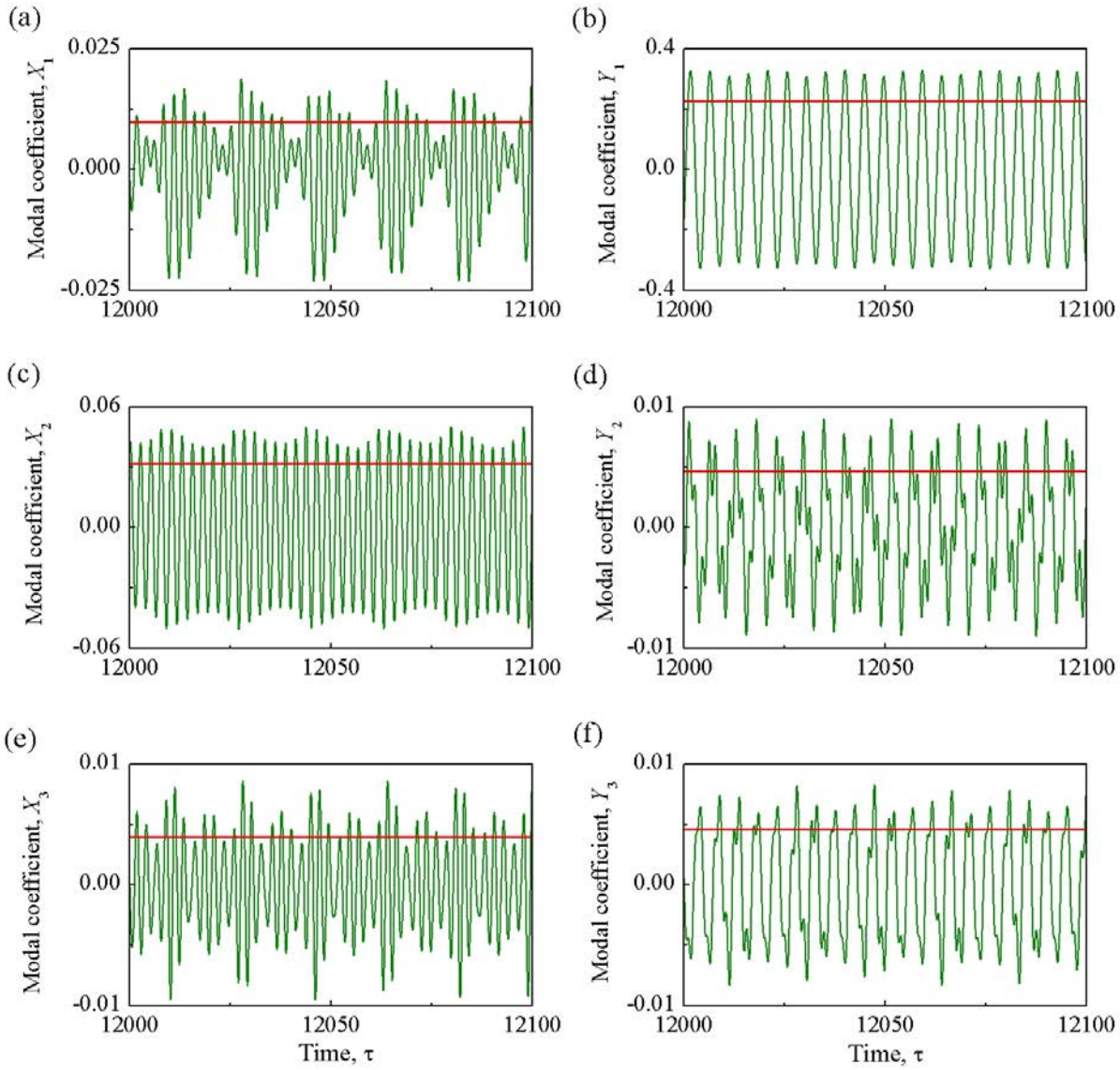

Figure 9: Time histories of amplitudes of the modal coefficients generated by the 3 modes approximation of the model with Krenk-Nielsen - Van der Pol damping at reduced velocity $U_R = 8.2$ corresponding to the green solution in Fig. 6: (a) modal coefficient X_1; (b) modal coefficient Y_1; (c) modal coefficient X_2; (d) modal coefficient Y_2; (e) modal coefficient X_3; (f) modal coefficient Y_3. Red line denotes the value of standard deviation of the signal.

6 Conclusions

Modelling a flexible structure capable of moving in two directions and interacting with the uniform flow was undertaken in this study. The main effort has been focused on the case of horizontally positioned structure. The proposed new models include wake oscillator equations containing various damping terms and used to simulate the fluid forces, similar to the ones successfully applied for the 2DOF rigid structure [5]. The calibration of the models has been performed using the techniques suggested and tested in [5] using the data [48] for the cross-flow displacements recorded at the middle of the structure. The properties of the calibrated model variations have been studied for three selected options, namely those containing Krenk-Nielsen - Van der Pol damping, Van der Pol - Van der Pol damping and Rayleigh - Rayleigh damping.

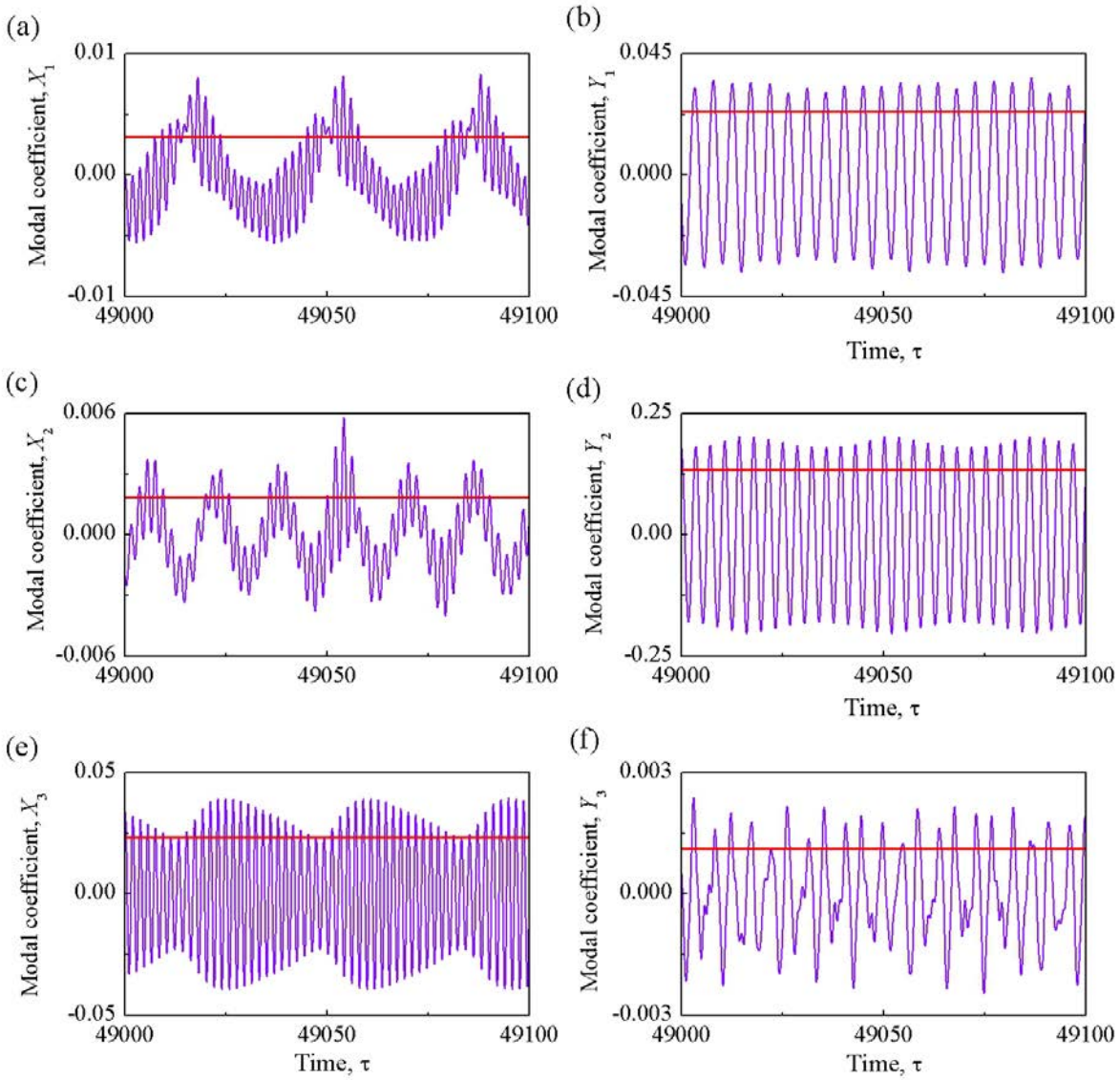

Figure 10: Time histories of amplitudes of the modal coefficients generated by the 3 modes approximation of the model with Krenk-Nielsen - Van der Pol damping at reduced velocity $U_R = 8.2$ corresponding to the violet solution in Fig. 6: (a) modal coefficient X_1; (b) modal coefficient Y_1; (c) modal coefficient X_2; (d) modal coefficient Y_2; (e) modal coefficient X_3; (f) modal coefficient Y_3. Red line denotes the value of standard deviation of the signal.

The detailed analysis of the model dynamics has been performed for the version of Krenk-Nielsen - Van der Pol dampings using 5 mode approximation and 3 mode approximation. The former has shown that a number of synchronization regions in the reduced velocity range coincides with the number of considered modes for the cross-flow displacement, whereas there are more synchronization regions for the in-line displacement amplitudes than the modes taken into account. The in-line displacement frequencies also demonstrated the presence of the dominating low frequencies in a few short ranges of the reduced velocity over the general trend of the growing frequencies.

A detailed consideration of the 3 mode approximation of the Krenk-Nielsen - Van der Pol model reveals a presence of co-existing solutions in a number of regions of the reduced velocity. They are observed clearly for the in-line displacement amplitudes and, respectively, for the in-line modal coefficients. The found solutions

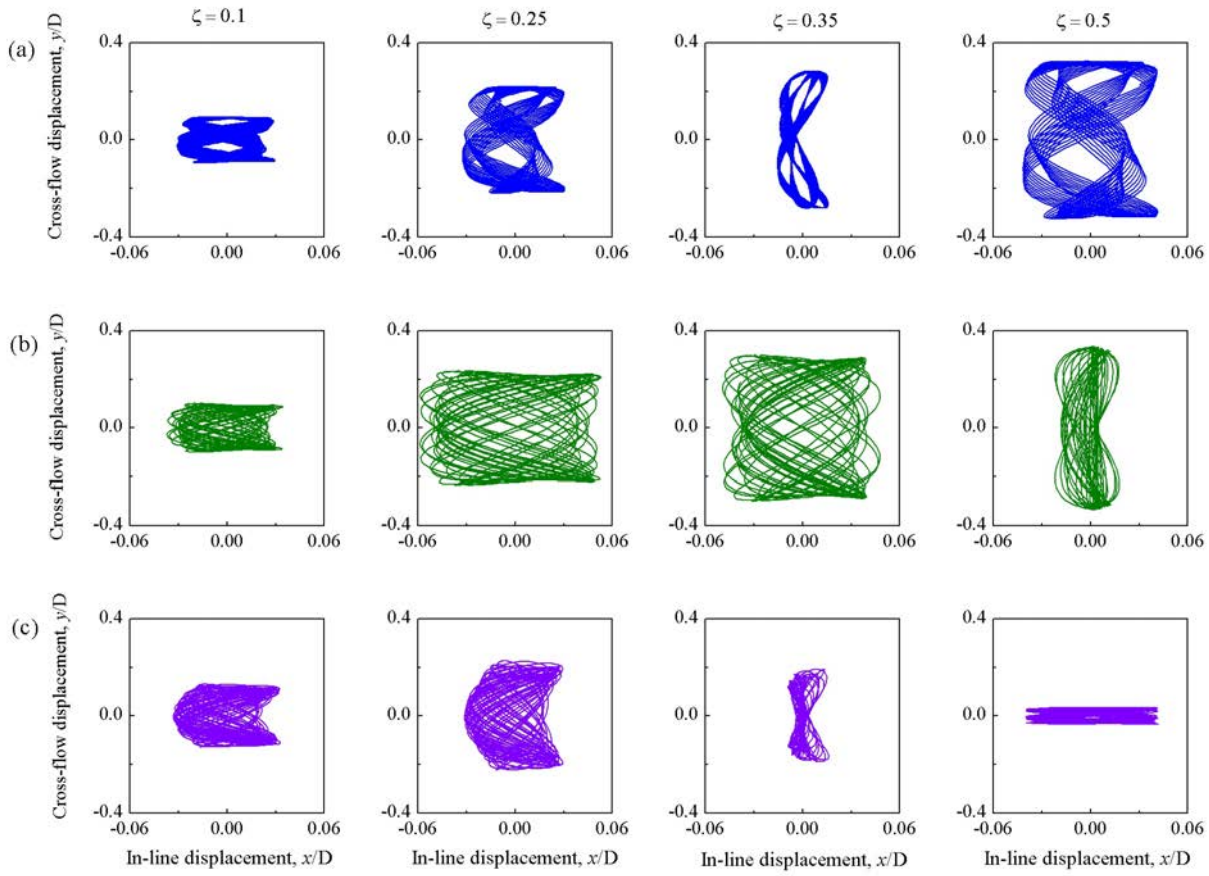

Figure 11: Cross-flow vs. in-line displacement amplitudes generated by the 3 modes approximation of the model with Krenk-Nielsen - Van der Pol damping at the beam cross-sections $\zeta = 0.10, 0.25, 0.35, 0.50$ at the reduced velocity $U_R = 8.2$: (a) trajectories corresponding to the blue solution in Fig. 6; (b) trajectories corresponding to the green solution in Fig. 6; (c) trajectories corresponding to the violet solution in Fig. 6.

demonstrate significant differences in the generated displacement amplitudes for the in-line direction and minor differences for the cross-flow direction. Some of these co-existing solution regions are located in between the peaks of the modal coefficient X_1. Our analysis also shows that using a standard deviation of the time histories of the modal coefficients generated by the model to represent the system response might not be always sufficient due to multiple frequencies present in the time histories. The dominating frequencies of the generated displacements at the cross-sections $\zeta = 0.25$, 0.35 and 0.50 demonstrate that some of the co-existing solutions have the frequencies significantly lower than the general trend in the intervals of the observed co-existence, but outside of those regions, some higher frequencies can be observed. It should be noted that co-existing responses of the rigid structure exhibiting flow-induced vibrations have been previously observed experimentally in [51] for the velocity ranges between VIV lock-in and galloping in the air. However further experimental investigations are required to verify a presence of the co-existing solutions in flexible structures.

The study revealed, that unlike the results for 2DOF rigid structures, both Van der Pol and Rayleigh damping terms appear to be applicable for predicting the behaviour of flexible structures experiencing VIV at this combination of the mass ratio of 1.17, the damping ratio of 0.024 and the Reynolds number range from 1780 to 14800. The results of the calibration procedure can be improved in the future, if any confirmed classification of experimental cases of vortex-induced vibrations of flexible structures or more results about the

in-line vibrations would be available.

The prospective future work should focus on the validation of the suggested and calibrated model for the cases of horizontally and vertically positioned structures. Also, the model should be expanded to include profiles of the flow velocity, and hence, become a tool to describe sheared flow cases.

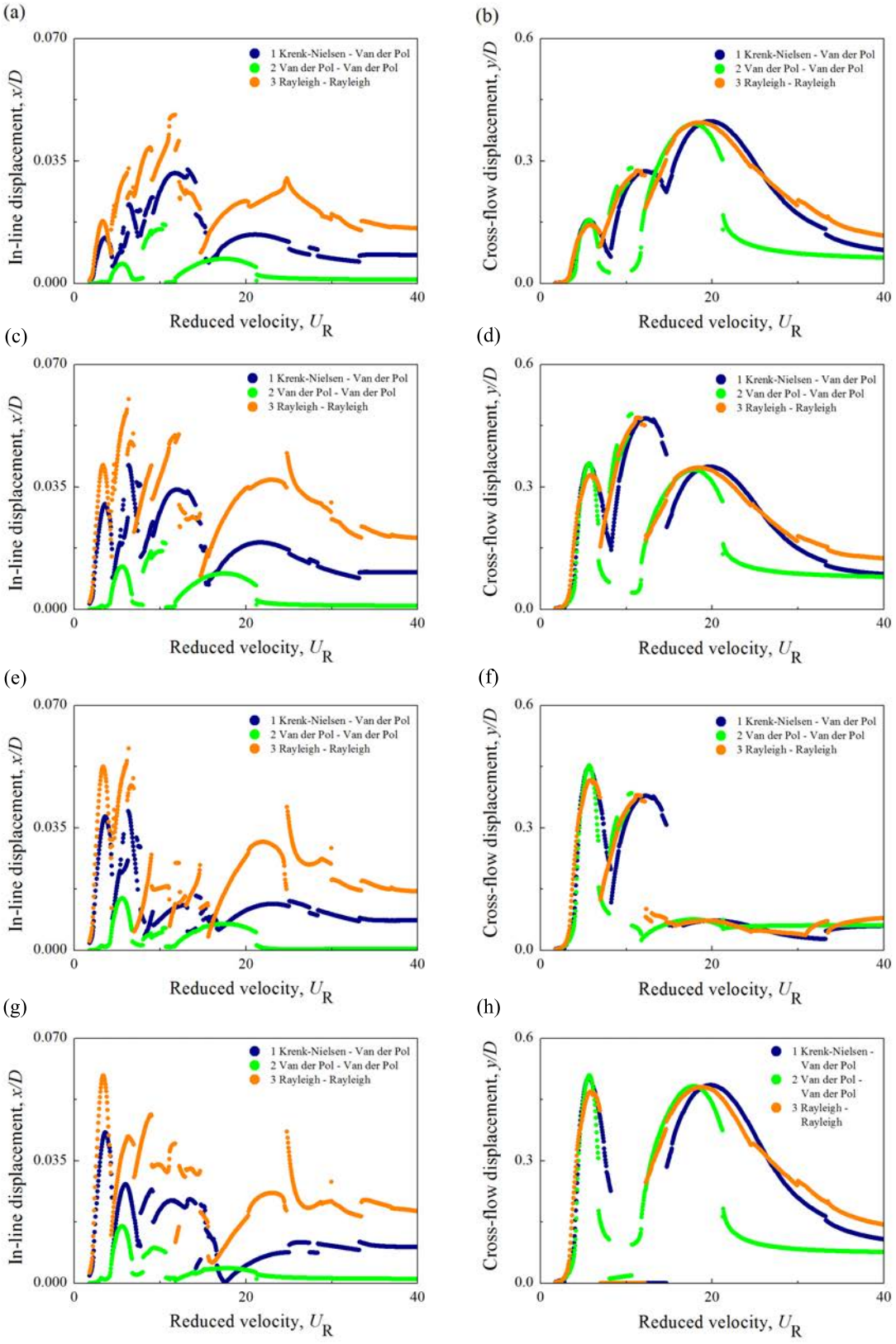

Figure 12: Displacement amplitudes over the reduced velocity range generated by the 3 mode approximations of the first three models from Table 4 in cross-sections: (a) in-line displacement in the cross-section $\zeta = 0.10$; (b) cross-flow displacement in the cross-section $\zeta = 0.10$; (c) in-line displacement in the cross-section $\zeta = 0.25$; (d) cross-flow displacement in the cross-section $\zeta = 0.25$; (e) in-line displacement in the cross-section $\zeta = 0.35$; (f) cross-flow displacement in the cross-section $\zeta = 0.35$; (g) in-line displacement in the cross-section $\zeta = 0.50$; (h) cross-flow displacement in the cross-section $\zeta = 0.50$.

References

[1] R.D. Blevins. Flow-induced vibration. Van Nostrand Reinhold Co., Inc., New York, NY (USA), 1990.

[2] R.D. Gabbai and H. Benaroya. An overview of modeling and experiments of vortex-induced vibration of circular cylinders. *Journal of Sound and Vibration*, 282(3–5):575 – 616, 2005.

[3] R. Govardhan and C.H.K. Williamson. Mean and fluctuating velocity fields in the wake of a freely-vibrating cylinder. *Journal of Fluids and Structures*, 15(3):489–501, 2001.

[4] N. Jauvtis and C.H.K. Williamson. The effect of two degrees-of-freedom on vortex-induced vibration at low mass and damping. *Journal of Fluid Mechanics*, 509:23–62, 2004.

[5] V. Kurushina, E. Pavlovskaia, A. Postnikov, and M. Wiercigroch. Calibration and comparison of viv wake oscillator models for low mass ratio structures. *International Journal of Mechanical Sciences*, 142:547–560, 2018.

[6] V. Kurushina and E. Pavlovskaia. Fluid nonlinearities effect on wake oscillator model performance. *MATEC Web of Conferences*, 148, 04002, 2018.

[7] J.K. Vandiver. Dimensionless parameters important to the prediction of vortex-induced vibration of long, flexible cylinders in ocean currents. *Journal of Fluids and Structures*, 7(5):423–455, 1993.

[8] Y. Modarres-Sadeghi, F. Chasparis, M.S. Triantafyllou, M. Tognarelli, and P. Beynet. Chaotic response is a generic feature of vortex-induced vibrations of flexible risers. *Journal of Sound and Vibration*, 330(11): 2565–2579, 2011.

[9] C.M. Alexander. The complex vibrations and implied drag of a long oceanographic wire in cross-flow. *Ocean Engineering*, 8(4):379–406, 1981.

[10] J.K. Vandiver, L. Ma, and Z. Rao. Revealing the effects of damping on the flow-induced vibration of flexible cylinders. *Journal of Sound and Vibration*, 433:29–54, 2018.

[11] A.L.C. Fujarra, C.P. Pesce, F. Flemming, and C.H.K. Williamson. Vortex-induced vibration of a flexible cantilever. *Journal of Fluids and Structures*, 15(3-4):651–658, 2001.

[12] L.K. Quen, A. Abu, N. Kato, P. Muhamad, A. Sahekhaini, and H. Abdullah. Investigation on the effectiveness of helical strakes in suppressing VIV of flexible riser. *Applied Ocean Research*, 44:82–91, 2014.

[13] J. Song, L. Lu, B. Teng, H. Park, G. Tang, and H. Wu. Laboratory tests of vortex-induced vibrations of a long flexible riser pipe subjected to uniform flow. *Ocean Engineering*, 38(11-12):1308–1322, 2011.

[14] B. Stappenbelt and F. Lalji. Vortex-induced vibration super-upper response branch boundaries. *International Journal of Offshore and Polar Engineering*, 18(02):99–105, 2008.

[15] J.R. Chaplin, P.W. Bearman, F.J. Huera-Huarte, and R.J. Pattenden. Laboratory measurements of vortex-induced vibrations of a vertical tension riser in a stepped current. *Journal of Fluids and Structures*, 21(1): 3–24, 2005.

[16] F.J. Huera-Huarte, Z.A. Bangash, and L.M. Gonzalez. Towing tank experiments on the vortex-induced vibrations of low mass ratio long flexible cylinders. *Journal of Fluids and Structures*, 48:81–92, 2014.

[17] E.D. Gedikli and J.M. Dahl. Mode excitation hysteresis of a flexible cylinder undergoing vortex-induced vibrations. *Journal of Fluids and Structures*, 69:308–322, 2017.

[18] E.D. Gedikli, D. Chelidze, and J.M. Dahl. Observed mode shape effects on the cortex-induced vibration of bending dominated flexible cylinders simply supported at both ends. *Journal of Fluids and Structures*, 81:399–417, 2018.

[19] G.R. Franzini, C.P. Pesce, R.T. Gonçalves, A.L.C. Fujarra, and P. Mendes. An experimental investigation on concomitant Vortex-Induced Vibration and axial top-motion excitation with a long flexible cylinder in vertical configuration. *Ocean Engineering*, 156:596–612, 2018.

[20] J. Wang, S. Fu, R. Baarholm, J. Wu, and C.M. Larsen. Fatigue damage induced by vortex-induced vibrations in oscillatory flow. *Marine Structures*, 40:73–91, 2015.

[21] E. Wang and Q. Xiao. Numerical simulation of vortex-induced vibration of a vertical riser in uniform and linearly sheared currents. *Ocean Engineering*, 121:492–515, 2016.

[22] E. Lehn. VIV suppression tests on high L/D flexible cylinders (main report). *ExxonMobil upstream research company*, 2003. URL: http://vivguest:vivdr@towtanknas.mit.edu/EM/URC%2010-m%20VIV%20Test%20Marintek%20Report.pdf. Online; accessed on 17 December 2018.

[23] M.-H. Chung. On characteristics of two-degree-of-freedom vortex induced vibration of two low-mass circular cylinders in proximity at low reynolds number. *Journal of Heat and Fluid Flow*, 65:220–245, 2017.

[24] K.R. Yu, A. Hay, D. Pelletier, and S. Etienne. Two degrees of freedom vortex-induced vibration responses with zero mass and damping at low reynolds number. *Journal of Fluids and Structures*, 83:218–237, 2018.

[25] A. Postnikov, E. Pavlovskaia, and M. Wiercigroch. 2DOF CFD calibrated wake oscillator model to investigate vortex-induced vibrations. *International Journal of Mechanical Sciences*, 127:176–190, 2017.

[26] Orcaflex. URL: https://www.orcina.com/SoftwareProducts/OrcaFlex/. Online; accessed on 14 February 2019.

[27] Shear7. VIV Response Prediction Program. URL: https://shear7.com/. Online; accessed on 14 February 2019.

[28] R.E.D. Bishop and A.Y. Hassan. The lift and drag forces on a circular cylinder oscillating in a flowing fluid. *Proceedings of the Royal Society of London A: Mathematical, Physical and Engineering Sciences*, 277 (1368):51–75, 1964.

[29] R.T. Hartlen and I.G. Currie. Lift-oscillator model of vortex-induced vibration. *Journal of the Engineering Mechanics Division*, 96(5):577–591, 1970.

[30] A.H. Nayfeh, F. Owis, and M.R. Hajj. A model for the coupled lift and drag on a circular cylinder. *ASME 2003 International Design Engineering Technical Conferences and Computers and Information in Engineering Conference*. 1289–1296, 2003.

[31] M.L. Facchinetti, E. De Langre, and F. Biolley. Coupling of structure and wake oscillators in vortex-induced vibrations. *Journal of Fluids and Structures*, 19(2):123–140, 2004.

[32] W.-J. Kim and N.C. Perkins. Two-dimensional vortex-induced vibration of cable suspensions. *Journal of Fluids and Structures*, 16(2):229–245, 2002.

[33] R.H.M. Ogink and A.V. Metrikine. A wake oscillator with frequency dependent coupling for the modeling of vortex-induced vibration. *Journal of Sound and Vibration*, 329(26):5452–5473, 2010.

[34] N. Srinil and H. Zanganeh. Modelling of coupled cross-flow/in-line vortex-induced vibrations using double Duffing and Van der Pol oscillators. *Ocean Engineering*, 53:83–97, 2012.

[35] R. Landl. A mathematical model for vortex-excited vibrations of bluff bodies. *Journal of Sound and Vibration*, 42(2):219–234, 1975.

[36] S. Krenk and S.R.K. Nielsen. Energy balanced double oscillator model for vortex-induced vibrations. *Journal of Engineering Mechanics*, 125(3):263–271, 1999.

[37] R.H.M. Ogink and A.V. Metrikine. A wake oscillator with frequency dependent tuning coefficients for the modeling of VIV. *ASME 2008 27th International Conference on Offshore Mechanics and Arctic Engineering*. pp. 943–952, 2008.

[38] V. Kurushina and E. Pavlovskaia. Wake oscillator equations in modelling vortex-induced vibrations at low mass ratios. *OCEANS 2017-Aberdeen*, pages 1–6, 2017.

[39] O. Shoshani. Deterministic and stochastic analyses of the lock-in phenomenon in vortex-induced vibration. *Journal of Sound and Vibration*, 434:17–27, 2018.

[40] K. Xu, Y. Ge, and D. Zhang. Wake oscillator model for assessment of vortex-induced vibration of flexible structures under wind action. *Journal of Wind Engineering and Industrial Aerodynamics*, 136:192–200, 2015.

[41] S. Srinivasan, V.D. Narasimhamurthy, and B.S.V. Patnaik. Reduced order modelling of two degree-of-freedom vortex induced vibrations of a circular cylinder. *Journal of Wind Engineering and Industrial Aerodynamics*, 175:342–351, 2018.

[42] N. Srinil, P.-A. Opinel, and F. Tagliaferri. Empirical sensitivity of two-dimensional nonlinear wake-cylinder oscillators in cross-flow/in-line vortex-induced vibrations. *Journal of Fluids and Structures*, 83:310–338, 2018.

[43] T. Leclercq and E. de Langre. Vortex-induced vibrations of cylinders bent by the flow. *Journal of Fluids and Structures*, 80:77–93, 2018.

[44] Y. Gao, L. Zou, Z. Zong, S. Takagi, and Y. Kang. Numerical prediction of vortex-induced vibrations of a long flexible cylinder in uniform and linear shear flows using wake oscillator model. *Ocean Engineering*, 171:157–171, 2019.

[45] E.W.C. Wong and D.K. Kim. A simplified method to predict fatigue damage of TTR subjected to short-term VIV using artificl neural network. *Advances in Engineering Software*, 126:100–109, 2018.

[46] E. Pavlovskaia, M. Keber, A. Postnikov, K. Reddington, and M. Wiercigroch. Multi-modes approach to modelling of vortex-induced vibration. *International Journal of Non-Linear Mechanics*, 80:40–51, 2016.

[47] M. Keber and M. Wiercigroch. Dynamics of a vertical riser with weak structural nonlinearity excited by wakes. *Journal of Sound and Vibration*, 315(3):685–699, 2008.

[48] B. Sanaati and N. Kato. A study on the effects of axial stiffness and pre-tension on VIV dynamics of a flexible cylinder in uniform cross-flow. *Applied Ocean Research*, 37:198–210, 2012.

[49] C.P. Sparks. *Fundamentals of marine riser mechanics: basic principles and simplified analyses.* PennWell Books, 2007.

[50] Andrey Postnikov. *Wake oscillator and CFD in modelling of VIVs.* PhD thesis, University of Aberdeen, 2016.

[51] C. Mannini, T. Massai, and A.M. Marra. Modelling the interference of vortex-induced vibrations and galloping for a slender rectangular prism. *Journal of Sound and Vibration*, 419:493–509, 2018.

Appendix A

All time histories presented in this Appendix are computed for the experimental reduced velocity $U_R = 14.6$ by the model version with Krenk-Nielsen - Van der Pol damping terms, Option 1 in Table 4.

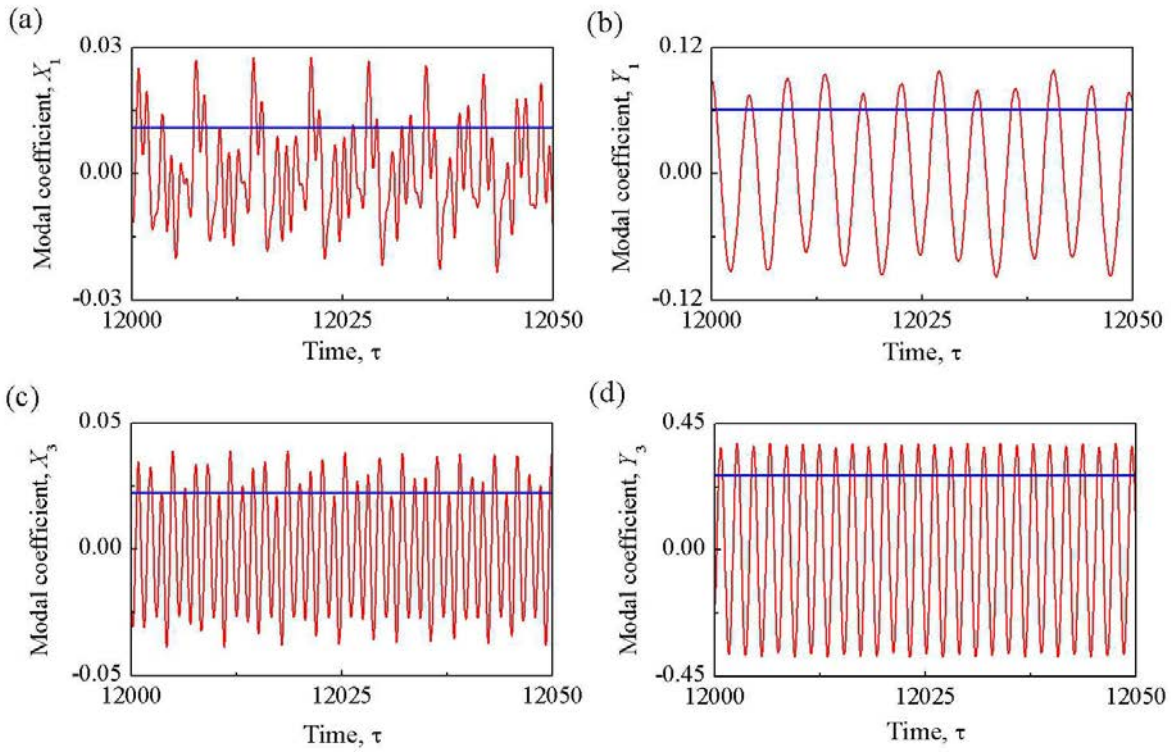

Figure 13: Time histories of amplitudes of the modal coefficients generated by the 3 modes approximation of the model with Krenk-Nielsen - Van der Pol damping at reduced velocity $U_R = 14.6$ corresponding to the red solution in Fig. 6: (a) modal coefficient X_1; (b) modal coefficient Y_1; (c) modal coefficient X_3; (d) modal coefficient Y_3. Blue line denotes the value of standard deviation of the signal. The modal coefficients X_2 and Y_2 have comparatively small values and are not presented in this figure.

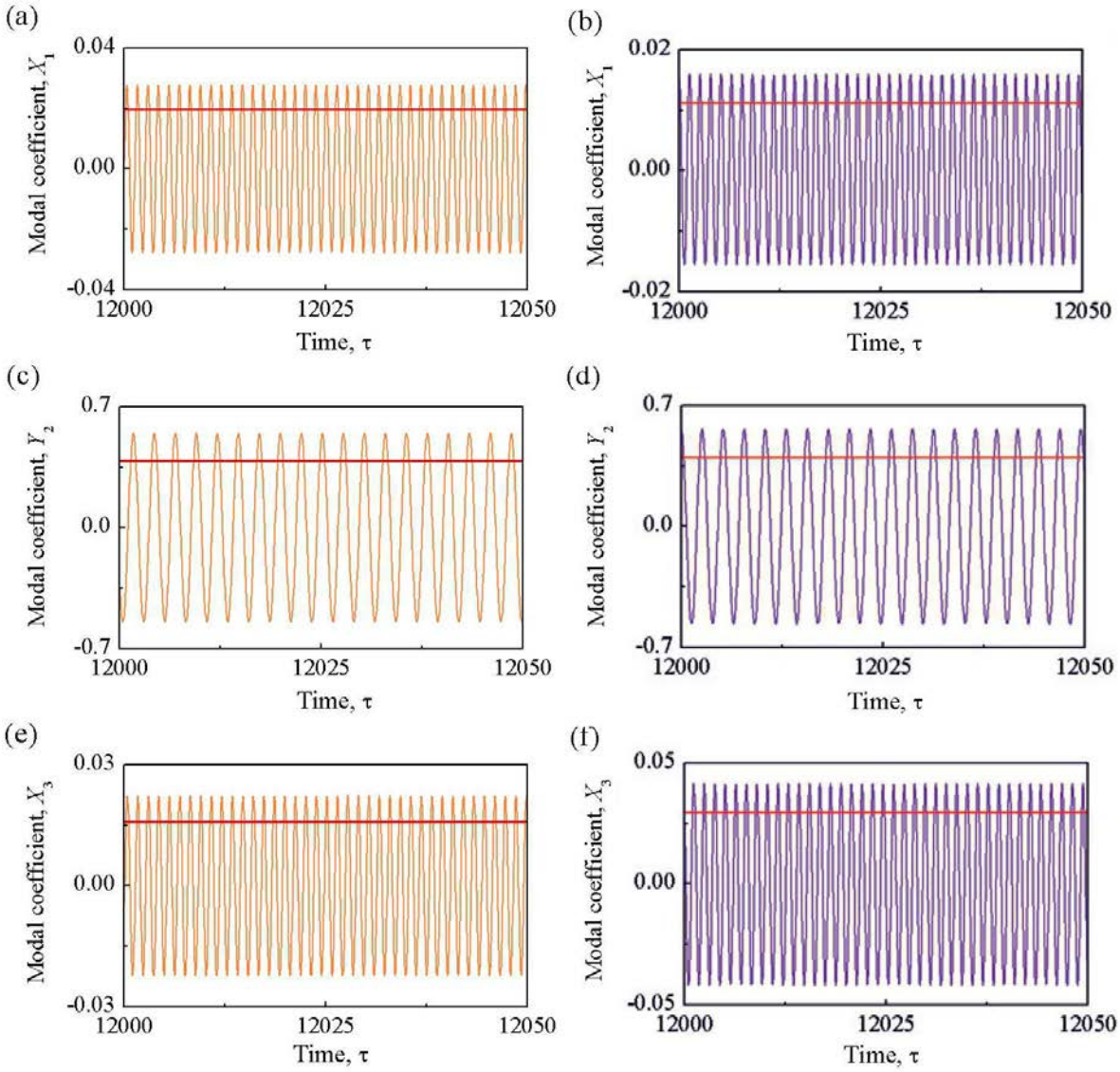

Figure 14: Time histories of amplitudes of the modal coefficients generated by the 3 modes approximation of the model with Krenk-Nielsen - Van der Pol damping at reduced velocity $U_R = 14.6$ corresponding to the solutions in Fig. 6: (a) modal coefficient X_1 corresponding to the orange solution; (b) modal coefficient X_1 corresponding to the violet solution; (c) modal coefficient Y_2 corresponding to the orange solution; (d) modal coefficient Y_2 corresponding to the violet solution; (e) modal coefficient X_3 corresponding to the orange solution; (f) modal coefficient Y_3 corresponding to the violet solution. Red line denotes the value of standard deviation of the signal. The modal coefficients Y_1, X_2 and Y_3 have comparatively small values in both solutions and are not presented in this figure.

Appendix B

Orbits presented in this Appendix are computed by the 3 modes approximation of the model with Krenk-Nielsen - Van der Pol damping for a number of reduced velocities and cross-sections.

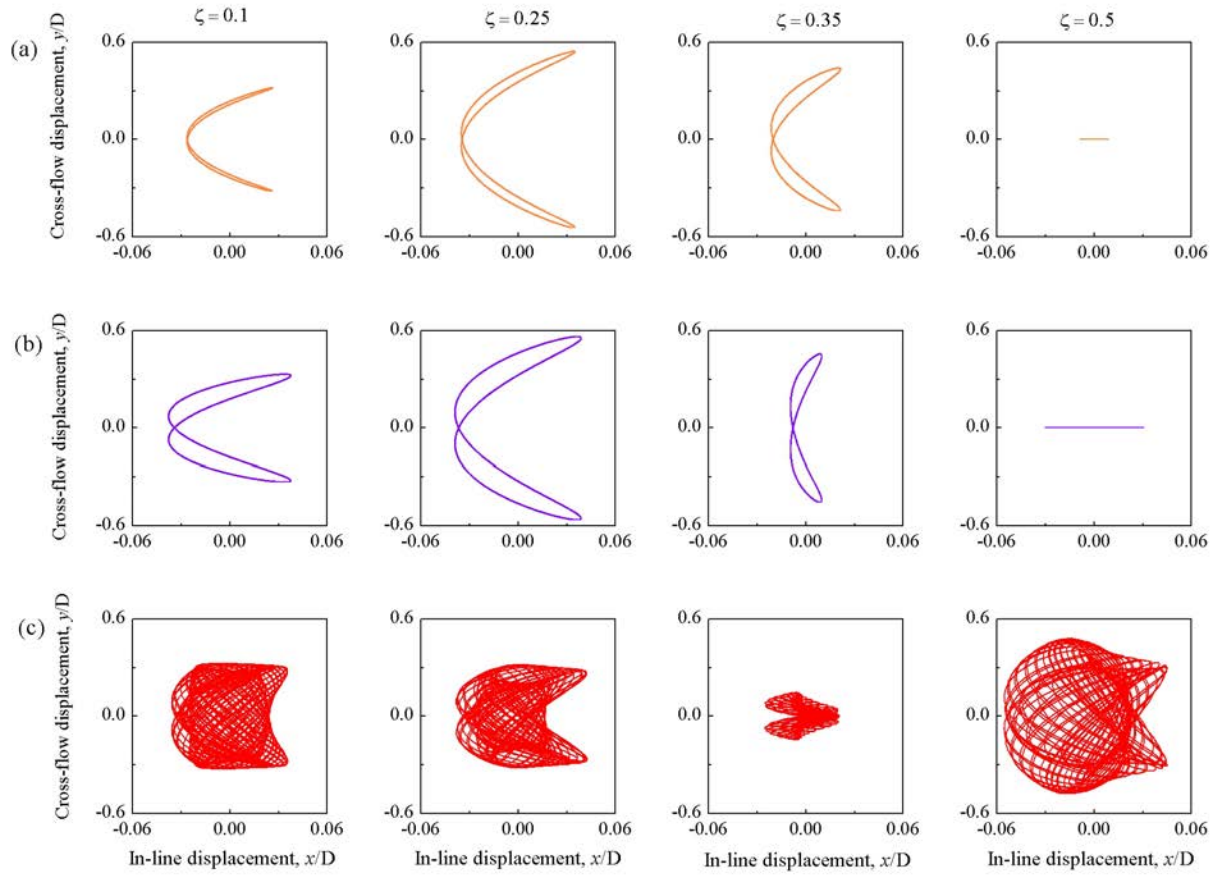

Figure 15: Cross-flow vs. in-line displacement amplitudes generated by the 3 modes approximation of the model with Krenk-Nielsen - Van der Pol damping at the beam cross-sections $\zeta = 0.10, 0.25, 0.35, 0.50$ at the reduced velocity $U_R = 14.6$: (a) trajectories corresponding to the orange solution in Fig. 6; (b) trajectories corresponding to the violet solution in Fig. 6; (c) trajectories corresponding to the red solution in Fig. 6.

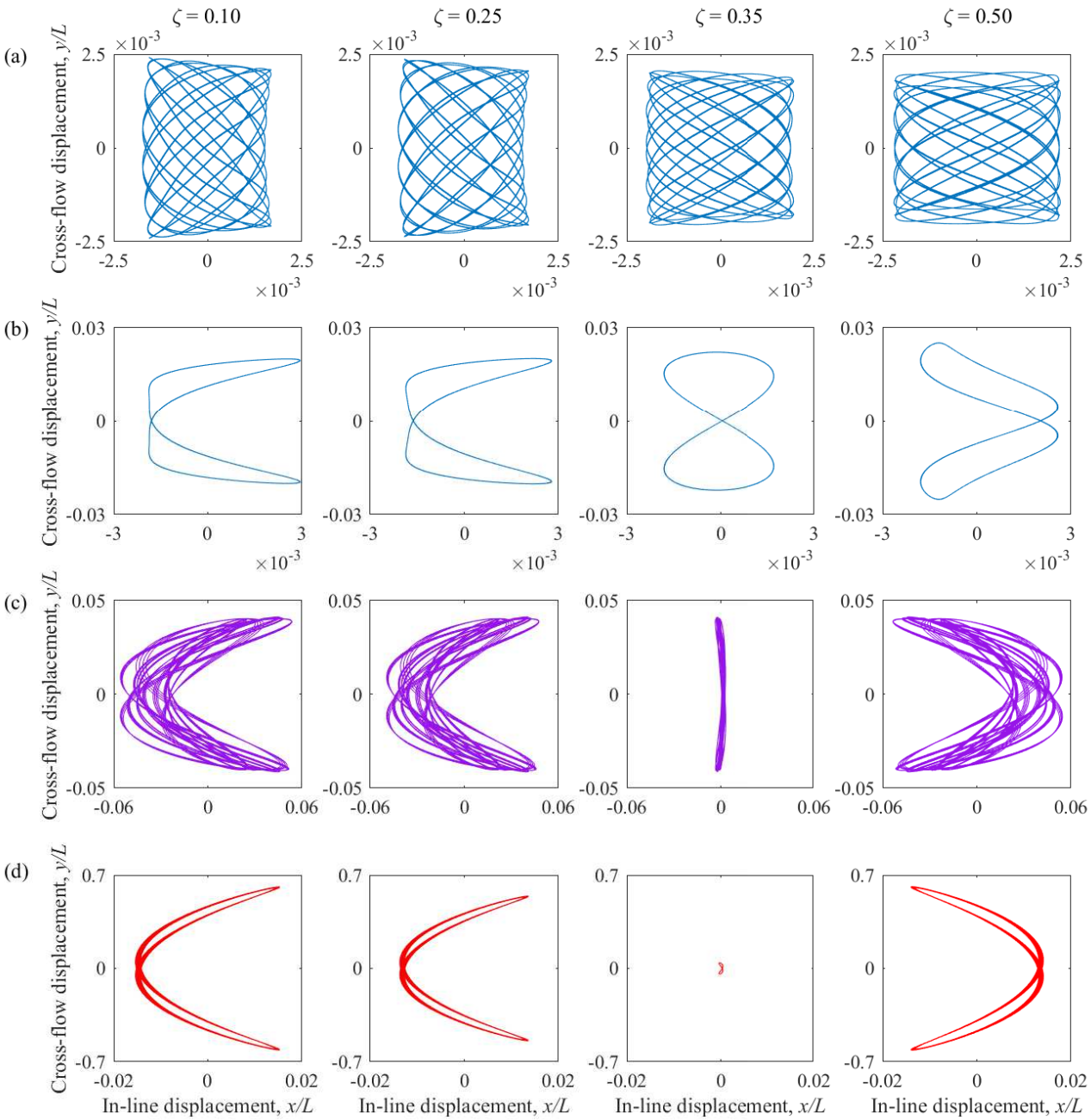

Figure 16: Trajectories of the in-line and cross-flow displacements generated by the model with Krenk-Nielsen - Van der Pol damping terms at the reduced velocities corresponding to the peaks of the modal coefficient $X1$ in Fig. 6a: (a) $U_R = 3.6$; (b) $U_R = 6.0$; (c) $U_R = 13.0$; (d) $U_R = 21.0$.